JOURNAL OF AIRCRAFT
Vol. 56, No. 4, July–August 2019

Observability and Performance Analysis of a Model-Free Synthetic Air Data Estimator

Kerry Sun,* Christopher D. Regan,† and Demoz Gebre-Egziabher‡
University of Minnesota, Twin Cities, Minneapolis, Minnesota 55455

DOI: 10.2514/1.C035290

The performance, accuracy, and observability of a model-free angle of attack and angle of sideslip estimator are presented. The estimator does not require an aircraft dynamic model; rather, it only relies on measurements from a GPS receiver, an inertial measurement unit, and a pitot tube. The estimator is an inertial navigation system (INS)/GPS extended Kalman filter augmented with the states to account for wind and an additional measurement from a pitot tube. It is shown that the estimator is conditionally observable. Conditions (maneuvers) that enhance its observability are identified. A bound on the angle of attack and angle of sideslip estimate uncertainties is derived. The effect of INS/GPS, horizontal and vertical wind uncertainty on the accuracy of angle of attack and angle of sideslip estimate is assessed. Simulation and flight-test results of the method are presented. The results show that the $1-\sigma$ bound on a small, slow-flying unmanned aerial vehicle for angle of attack and sideslip angle estimates are about 5 and 3 deg, respectively.

Nomenclature

$\boldsymbol{A}_{\alpha\beta}$ = flow angle sensitivity matrix
a_x, a_y, a_z = accelerometer components
b_{ax}, b_{ay}, b_{az} = gyro biases
b_{gx}, b_{gy}, b_{gz} = accelerometer biases
C_b^n = direction cosine matrix from body frame to north–east–down frame
$\mathcal{G}_d$ = discrete observability gramian
$\boldsymbol{H}$ = linearized Jacobian measurement matrix
$\boldsymbol{O}$ = observability matrix
$\boldsymbol{P}$ = state error covariance matrix
P_N, P_E, P_D = components of north–east–down position, m
$\boldsymbol{P}_{\alpha\beta}$ = flow angle error covariance matrix
$\boldsymbol{R}$ = measurement noise matrix
u, v, w = components of airspeed velocity in the body frame, m/s
u_g, v_g, w_g = components of airspeed velocity in the north–east–down frame, m/s
V_a = airspeed magnitude, m/s
$\boldsymbol{V}_a$ = airspeed vector
V_N, V_E, V_D = components of inertial velocity, m/s
W_N, W_E, W_D = components of wind velocity, m/s
$\boldsymbol{w}$ = process noise vector
$\boldsymbol{x}$ = state vector
$\boldsymbol{y}$ = measurement vector
α, β = angle of attack and angle of sideslip
$\boldsymbol{\eta}$ = measurement noise vector
κ = condition number
$\sigma_{(\cdot)}$ = standard deviation
$\tau_{(\cdot)}$ = correlation time constant (a first-order Gauss–Markov process)
$\boldsymbol{\Phi}$ = state-transition matrix
ϕ, θ, ψ = roll, pitch, and yaw angles

Subscripts

ad = accelerometer dynamic (time-varying) output error
aw = accelerometer white (uncorrelated) output error
gd = gyro dynamic (time-varying) output error
gw = gyro white (uncorrelated) output error
m = measured quantity

Superscripts

b = quantity in the body frame
L = lower bound
n = quantity in the north–east–down frame
U = upper bound

I. Introduction

AN AIRCRAFT'S performance and safety in flight depend, in part, on the magnitude of airspeed V_a and the orientation of the aircraft, as quantified by angle of attack α and angle of sideslip β. Accurate estimates of these parameters are essential for the efficient and safe operation of aircraft. Traditionally, V_a, α, and β are directly measured by sensors, but there is new interest in methods for indirectly estimating them. For example, because many small unmanned aerial vehicle (UAV) systems cannot accommodate sensors that directly measure these quantities due to size, weight, and power constraints (e.g., wind vanes), nontraditional approaches collectively known as synthetic air data systems are being considered [1]. Synthetic air data systems (SADS), in short, are algorithms for generating estimates of the air data triplets V_a, α, and β indirectly without using the traditional air data sensors such as pitot tubes and vanes. The current state-of-the-art synthetic air data systems use a high-fidelity vehicle dynamics model fused with inertial measurement unit (IMU) and GPS measurements to estimate V_a, α, and β [1–6]. However, a high-fidelity aircraft model is difficult to obtain, and the parameters of the aircraft model can change over time due to wear and tear of the airframe and propulsion system [1]. This makes model-free synthetic air data estimation methods an attractive alternative [7]. A model-free system would be particularly useful for system identification of small UAVs. In these applications, the aircraft dynamic model is the unknown that needs to be determined, and algorithms for doing this can greatly benefit from the availability of α and β estimates [8]. Another potential application for model-free approaches is fault detection and isolation of traditional air data system malfunctions [9–12].

Received 8 October 2018; revision received 13 January 2019; accepted for publication 29 January 2019; published online 14 March 2019.

*Graduate Research Assistant, Department of Aerospace Engineering and Mechanics; sunx0486@umn.edu. Student Member AIAA.

†Research Fellow, Department of Aerospace Engineering and Mechanics; rega0051@umn.edu.

‡Professor, Department of Aerospace Engineering and Mechanics; gebre@umn.edu. Associate Fellow AIAA.

A. Prior Work

Some of the earlier SADS literature relevant to the work here is from the late 1980s. In these works, the idea to use non-air-data sensors such as IMU and GPS fused with vehicle dynamics models to estimate the air data triplet V_a, α, and β (either separately or combined) is explained. Most of the earlier work used vehicle dynamics models to estimate air data in both aircraft and spacecraft applications. We refer to this approach as the aerodynamic model-based SADS [1,2,6,13–22]. The aerodynamic model-based SADS are difficult to implement, however, because it is challenging to obtain accurate vehicle dynamics models possessing the fidelity needed to yield the required accuracy in α, β, and V_a estimates. To address this issue, model-free SADS have been proposed [4,5,7,23]. There are a couple of key challenges in the model-free SADS framework. First, an accurate three-dimensional (3-D) wind vector estimate is needed for the model-free SADS. In most of the previous work, either wind modeling was not considered [23], or the wind modeling is two-dimensional (horizontal wind only) [24]. Furthermore, most of the wind estimators require an aircraft dynamics model [25,26]. Another challenge that has not been addressed adequately in the literature is the observability issue. Showing under what conditions the estimator is observable has not been studied extensively. In the Kalman filtering setting, observability analysis is often used as a binary test to show whether a system is observable or not [27–30]. However, in the SADS problem, this is not sufficient because the fact that a system is observable does not guarantee that the state estimates will be accurate. This is the problem of quantifying observability, and there has been some recent work in this area [31–34]. Most of the work, however, analyzes observability as a function of the vehicle trajectory ex post facto instead of giving guidance as to what flight maneuver sequences to execute to enhance observability.

B. Contribution

There are two objectives of this paper. First, building on work first reported in [7], we will show that it is possible to design a model-free SADS estimator that can generate sufficiently accurate estimates of α, β, and 3-D wind vector without using an aerodynamic model of the aircraft. Second, we will present a covariance analysis that quantifies the accuracy of the model-free estimator as a function of inputs (e.g., sensor noise, vehicle maneuvers, etc.). To address the first objective, we show that the model-free SADS estimator is conditionally observable under the slow-varying wind assumption. A linear time-varying (LTV) observability analysis is also constructed to examine the flight maneuver sequence that yields a high degree of observability. The findings of this observability analysis are validated using simulation and experimental flight-test data. Related to the second objective, the covariance bounds for α and β are derived using the general law of propagation variances [35]. Monte Carlo analysis is performed on several parameters, including IMU and GPS sensor errors, to show how various error sources affect the accuracy of α and β.

C. Paper Organization

The remainder of this paper is organized as follows. Section II presents a brief description of the model-free SADS estimator developed in this paper. Sections III and IV present the observability analysis for the estimator. Section V presents simulation results assessing the estimator's performance, and Sec. VI addresses the limitations on the model-free estimator. In Sec. VII, the estimator is validated using flight-test data from a small UAV.

II. Estimator Description

In this section, a brief overview of the time update and measurement models for the model-free air data estimator is provided. The estimator is an extension of the 15-state, loosely coupled inertial navigation system (INS)/GPS extended Kalman filter (EKF) [36], which blends information from an IMU and GPS receiver. The INS/GPS filter's state vector is augmented by three additional states representing the components of the wind velocity vector. Therefore, the SADS filter state vector $\delta \boldsymbol{x} \in \mathbb{R}^{18\times 1}$ is given by

$$\delta \boldsymbol{x} = [\,\delta \boldsymbol{p}^n \quad \delta \boldsymbol{v}^n \quad \delta \boldsymbol{\varepsilon} \quad \delta \boldsymbol{b}_a \quad \delta \boldsymbol{b}_g \quad \delta \boldsymbol{W}^n\,]^T \tag{1}$$

where $\delta \boldsymbol{p}^n = [\,\delta P_N \quad \delta P_E \quad \delta P_D\,]^T$ and $\delta \boldsymbol{v}^n = [\,\delta V_N \quad \delta V_E \quad \delta V_D\,]^T$ are the position and velocity error vectors resolved in the north–east–down (NED) frame. The vector $\delta \boldsymbol{\varepsilon} = [\,\delta \varepsilon_N \quad \delta \varepsilon_E \quad \delta \varepsilon_D\,]^T$ represents the attitude errors, which are defined to be the small rotations between the actual NED frame and the estimated NED frame. The vectors $\delta \boldsymbol{b}_a = [\,\delta b_{ax} \quad \delta b_{ay} \quad \delta b_{az}\,]^T$ and $\delta \boldsymbol{b}_g = [\,\delta b_{gx} \quad \delta b_{gy} \quad \delta b_{gz}\,]^T$ are accelerometer and rate gyro triad output errors (bias). Finally, $\delta \boldsymbol{W}^n = [\,\delta W_N \quad \delta W_E \quad \delta W_D\,]^T$ is the error in the wind speed vector resolved about the NED frame.

The estimates of α and β are calculated using the following:

$$\alpha = \tan^{-1}\left(\frac{u}{v}\right), \qquad \beta = \sin^{-1}\left(\frac{v}{\sqrt{u^2 + v^2 + w^2}}\right) \tag{2}$$

where

$$[\,u \quad v \quad w\,]^T = \boldsymbol{C}_n^b[\boldsymbol{v}^n - \boldsymbol{W}^n] \tag{3}$$

and $\boldsymbol{C}_n^b = [\boldsymbol{C}_b^n]^T$. The measurement vector $\boldsymbol{y} \in \mathbb{R}^{7\times 1}$ consists of GPS position and velocity estimates along with the scalar airspeed V_a; it is given by

$$\boldsymbol{y} = [\,\boldsymbol{p}^n \quad \boldsymbol{v}^n \quad V_a\,]^T \tag{4}$$

where V_a is the true airspeed estimate determined using the pressure measurements from a pitot tube. Figure 1 shows the overall filter architecture. The time and covariance update equations for this filter are, for the most part, identical to those of the filter described in [36]. What is new is the dynamic model for the augmented states (wind) and the measurement model. Similar to the modeling of the accelerometer and gyroscope biases in the filter, the dynamics of the wind is modeled as a first-order Gauss–Markov model, motivated by [37]. The details of the Gauss–Markov model for the wind and sensors can be found in [37,38], respectively.

The linearized measurement error model used by the EKF is $\delta \boldsymbol{y}_i = \boldsymbol{y}_i - \hat{\boldsymbol{y}}_i \approx \boldsymbol{H}_i \delta \boldsymbol{x}_i + \boldsymbol{\eta}_i$. Note that $V_a = \|\boldsymbol{v}^n - \boldsymbol{W}^n\|_2 + \eta_{V_a}$,

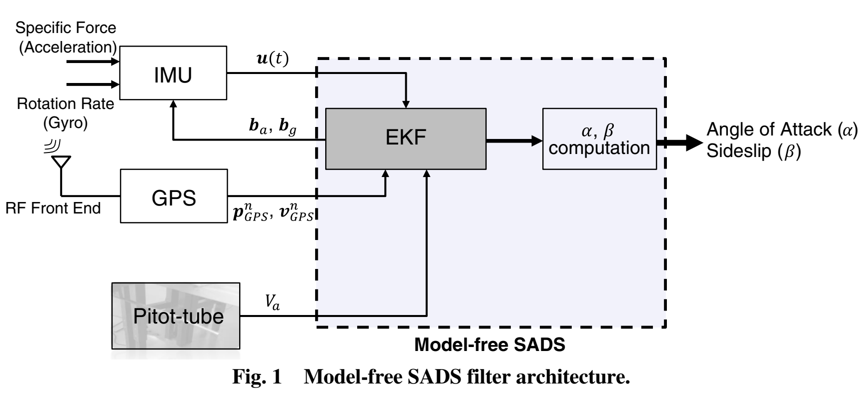

Fig. 1 Model-free SADS filter architecture.

and $\hat{\boldsymbol{y}}_i$ is the predicted measurement. The measurement Jacobian $\boldsymbol{H}_i \in \mathbb{R}^{7\times 18}$ is given by the following:

$$\boldsymbol{H}_i = \begin{bmatrix} \boldsymbol{I}_3 & \boldsymbol{0}_3 & \boldsymbol{0}_{3\times 9} & \boldsymbol{0}_3 \\ \boldsymbol{0}_3 & \boldsymbol{I}_3 & \boldsymbol{0}_{3\times 9} & \boldsymbol{0}_3 \\ \boldsymbol{0}_1 & H_{v^n} & \boldsymbol{0}_{1\times 9} & H_{W^n} \end{bmatrix} \tag{5}$$

where H_{v^n} can be calculated as

$$H_{v^n} = \frac{1}{V_a}[\, V_N - W_N \quad V_E - W_E \quad V_D - W_D \,] \tag{6}$$

and $H_{W^n} = -H_{v^n}$. The measurement noise $\boldsymbol{\eta}$ is modeled as a zero mean, white Gaussian sequence with a diagonal covariance $\boldsymbol{R}$. That is,

$$\boldsymbol{R} = \mathrm{diag}([\, \sigma_{P_N}^2 \quad \sigma_{P_E}^2 \quad \sigma_{P_D}^2 \quad \sigma_{V_N}^2 \quad \sigma_{V_E}^2 \quad \sigma_{V_D}^2 \quad \sigma_{V_a}^2 \,]) \tag{7}$$

The estimates and covariances of α and β are computed at each time step as illustrated by the α, β computation block in Fig. 1. Note that α and β are not part of the EKF state vector. Rather, they are functions of the EKF state vector, as given in Eqs. (2) and (3). Their covariance matrix $\boldsymbol{P}_{\alpha\beta}$ is computed using the general law of propagation variances [35] as follows:

$$\boldsymbol{P}_{\alpha\beta} = A_{\alpha\beta}\boldsymbol{P}A_{\alpha\beta}^T \tag{8}$$

where $\boldsymbol{P} \in \mathbb{R}^{18\times 18}$ is the covariance matrix of the EKF, and $A_{\alpha\beta} \in \mathbb{R}^{2\times 18}$ is the flow angle sensitivity matrix given by

$$A_{\alpha\beta} = \begin{bmatrix} \frac{\partial\alpha}{\partial P_N} & \frac{\partial\alpha}{\partial P_E} & \frac{\partial\alpha}{\partial P_D} & \frac{\partial\alpha}{\partial V_N} & \frac{\partial\alpha}{\partial V_E} & \frac{\partial\alpha}{\partial V_D} & \frac{\partial\alpha}{\partial\phi} & \frac{\partial\alpha}{\partial\theta} & \frac{\partial\alpha}{\partial\psi} & \frac{\partial\alpha}{\partial b_{ax}} & \frac{\partial\alpha}{\partial b_{ay}} & \frac{\partial\alpha}{\partial b_{az}} & \frac{\partial\alpha}{\partial b_{gx}} & \frac{\partial\alpha}{\partial b_{gy}} & \frac{\partial\alpha}{\partial b_{gz}} & \frac{\partial\alpha}{\partial W_N} & \frac{\partial\alpha}{\partial W_E} & \frac{\partial\alpha}{\partial W_D} \\ \frac{\partial\beta}{\partial P_N} & \frac{\partial\beta}{\partial P_E} & \frac{\partial\beta}{\partial P_D} & \frac{\partial\beta}{\partial V_N} & \frac{\partial\beta}{\partial V_E} & \frac{\partial\beta}{\partial V_D} & \frac{\partial\beta}{\partial\phi} & \frac{\partial\beta}{\partial\theta} & \frac{\partial\beta}{\partial\psi} & \frac{\partial\beta}{\partial b_{ax}} & \frac{\partial\beta}{\partial b_{ay}} & \frac{\partial\beta}{\partial b_{az}} & \frac{\partial\beta}{\partial b_{gx}} & \frac{\partial\beta}{\partial b_{gy}} & \frac{\partial\beta}{\partial b_{gz}} & \frac{\partial\beta}{\partial W_N} & \frac{\partial\beta}{\partial W_E} & \frac{\partial\beta}{\partial W_D} \end{bmatrix} \tag{9}$$

The partial derivatives with respect to the position $\boldsymbol{p}^n$, accelerometer $\boldsymbol{b}_a$, and gyro $\boldsymbol{b}_g$ biases are zero (see the Appendix). Therefore, the covariance of α and β depends on the covariance of the inertial velocity, attitude, and 3-D wind estimates. The matrix $A_{\alpha\beta}$ will be used in Sec. VI for error analysis.

III. Observability Analysis

In [7], it was shown that the SADS estimator is conditionally observable. For completeness, we will briefly discuss the results of the observability analysis from [7] because its results are a prerequisite for understanding the observability enhancement results discussed later in the paper. Recall that the mathematical models in the synthetic air data estimation problem [the INS/GPS equations in [36], Eqs. (2) and (3)] are nonlinear. The formulation of the EKF requires linearizing the mathematical models, and thus the resulting estimator falls in the domain of linear time-varying systems. Therefore, the observability analysis requires the combined use of nonlinear and linear tools. In this paper, we take a two-tiered approach to this analysis. The first tier involves assessing the observability of the state vector $\delta\boldsymbol{x} \in \mathbb{R}^{18\times 1}$ given by Eq. (1). This analysis was carried out in some detail in [7], and the details of that analysis will not be repeated here. The key results of this analysis were that $\delta\boldsymbol{x}$ is conditionally observable and its observability requires the following.

1) The airplane is accelerating so that the INS/GPS heading and gyro bias states become observable [36].

2) The wind speed vector $\boldsymbol{W}^n$ is quasi-static. The term quasi-static is used to mean that the variations in $\boldsymbol{W}^n$ are such that it is valid to assume that it remains constant over a small time window.

With respect to the second observability condition, the size of the time window in which $\boldsymbol{W}^n$ can be assumed constant depends on several factors. In the second-tier analysis (see Sec. IV), we provide mathematical relationships describing these and other conditions that enhance the observability of the SADS estimates.

IV. Observability Enhancement

Although the work in [7] provided a mathematically based observability analysis, the second-tiered analysis here will provide a more intuitive interpretation. The goal is to get insight into how observability can be improved or enhanced. This approach sheds some light on how to design flight maneuver sequences to optimize the degree of observability. To this end, the estimation problem is recast in a slightly different way. The objective is to estimate α, β, W_N, W_E, and W_D. Observability is an inherent property of the system that does not change by new definitions of the state vector. The recasting does not alter the observability, but it gives a better view into the problem by essentially eliminating the dynamic model and allowing us to recast the problem as a batch estimation process.

A. Change of Variables

Let $\boldsymbol{v}_g^b = [\, u_g \quad v_g \quad w_g \,]^T$ denote the velocity vector of the aircraft ground velocity in the body frame. Let $\boldsymbol{v}_a^b = [\, u \quad v \quad w \,]^T$ be the air velocity in the body frame. The kinematic relationship between ground velocity, air velocity, and wind velocity is described by the following:

$$\begin{bmatrix} u_g \\ v_g \\ w_g \end{bmatrix} = \begin{bmatrix} u \\ v \\ w \end{bmatrix} + \boldsymbol{C}_n^b \begin{bmatrix} W_N \\ W_E \\ W_D \end{bmatrix} \tag{10}$$

The vector $\boldsymbol{v}_a^b$ can also be expressed in terms of airspeed V_a, angle of attack α, and side-slip angle β, as shown in Eq. (11):

$$\begin{bmatrix} u \\ v \\ w \end{bmatrix} = \begin{bmatrix} V_a \cos\alpha\cos\beta \\ V_a \sin\beta \\ V_a \sin\alpha\cos\beta \end{bmatrix} \tag{11}$$

Note that $V_a \neq u$ because the stagnation pressure sensed by a pitot tube is relatively constant under small ($\leq \pm 10$ deg) variations of α and β [39].

Using a small-angle approximation for α and β and substituting Eq. (11) into Eq. (10) gives the following:

$$\begin{bmatrix} u_g - V_a \\ v_g \\ w_g \end{bmatrix} \approx \begin{bmatrix} 0 \\ V_a\beta \\ V_a\alpha \end{bmatrix} + C_n^b \begin{bmatrix} W_N \\ W_E \\ W_D \end{bmatrix} = [\boldsymbol{\Psi} \mid \boldsymbol{\Omega}] \begin{bmatrix} \boldsymbol{W}^n \\ \hline \alpha \\ \beta \end{bmatrix} \tag{12}$$

where $\boldsymbol{\Psi} = C_n^b$, and $\boldsymbol{\Omega}$ is a function of V_a, shown next:

$$\boldsymbol{\Omega} = \boldsymbol{\Omega}(V_a) = V_a \begin{bmatrix} 0 & 0 \\ 0 & 1 \\ 1 & 0 \end{bmatrix} \tag{13}$$

We will refer to Eq. (12) as the wind triangle kinematic relationship and use it as the measurement update equation of the following LTV system:

$$\mathrm{LTV}_K = \begin{cases} \boldsymbol{x}_{k+1} = \Phi_k \boldsymbol{x}_k + G_k \boldsymbol{u}_k + \boldsymbol{w}_k \\ \boldsymbol{y}_{k+1} = H_k \boldsymbol{x}_k + \boldsymbol{\eta}_k \end{cases} \tag{14}$$

where $H_k = [\boldsymbol{\Psi}_k \mid \boldsymbol{\Omega}_k]$; $\boldsymbol{y}_k = [u_g(k) - V_a(k) \quad v_g(k) \quad w_g(k)]^T$; the lowercase k represents the time step (sensor sampling rate); and the uppercase K represents the Kth piecewise LTV system (see Sec. IV.E.1). The states of the LTV are $\boldsymbol{x}_k = [W_N \quad W_E \quad W_D \quad \alpha_k \quad \beta_k]^T$. We assume that the wind is constant for each LTV, but α and β are not. Because we are performing a nonstochastic observability analysis, the process noise $\boldsymbol{w}_k$ and measurement noise $\boldsymbol{\eta}_k$ are dropped. Also, there is no input to the system (i.e., $G_k = 0$). Our objective is to convert this LTV into a batch process. To this, we can assume that Φ_k is equal to a 5×5 identity matrix. Because we have already assumed that the winds are constant in a given LTV, the fact that $\Phi_k = I_{5\times5}$ implies that all the information about the changes in α and β are coming from the measurement update equation of the LTV, namely Eq. (12).

To convert any LTV to a batch process, we assume that wind is constant over a time window of width $l \cdot T_s$. The constant l is the number of time steps ($l \in [1, 2, \ldots, k, \ldots, n-1, n]$), and $T_s = t_k - t_{k-1}$ is the sampling interval. Now, the entire trajectory is a collection of piecewise LTV systems $\mathrm{LTV}_1, \mathrm{LTV}_2, \ldots \mathrm{LTV}_K, \ldots \mathrm{LTV}_N$, where $K \in [1, N]$, and the wind vector is assumed to be constant over the time span $l \cdot T_s$. If we now start stacking the measurement equation for several epochs, we obtain

$$\underbrace{\begin{bmatrix} \boldsymbol{y}_1 \\ \boldsymbol{y}_2 \\ \boldsymbol{y}_3 \\ \vdots \\ \boldsymbol{y}_n \end{bmatrix}}_{\mathcal{Y}} = \underbrace{\begin{bmatrix} \boldsymbol{\Psi}_1 & \boldsymbol{\Omega}_1 & \boldsymbol{0}_{3\times2} & \cdots & \cdots & \boldsymbol{0}_{3\times2} \\ \boldsymbol{\Psi}_2 & \boldsymbol{0}_{3\times2} & \boldsymbol{\Omega}_2 & \boldsymbol{0}_{3\times2} & \cdots & \boldsymbol{0}_{3\times2} \\ \boldsymbol{\Psi}_3 & \boldsymbol{0}_{3\times2} & \boldsymbol{0}_{3\times2} & \boldsymbol{\Omega}_3 & \cdots & \boldsymbol{0}_{3\times2} \\ \vdots & \vdots & \vdots & \vdots & \vdots & \vdots \\ \boldsymbol{\Psi}_n & \cdots & \cdots & \cdots & \cdots & \boldsymbol{\Omega}_n \end{bmatrix}}_{\mathcal{H}} \underbrace{\left[\begin{array}{c} \boldsymbol{W}^n \\ \hline \alpha_1 \\ \beta_1 \\ \hline \alpha_2 \\ \beta_2 \\ \hline \alpha_3 \\ \beta_3 \\ \hline \vdots \\ \alpha_n \\ \beta_n \end{array}\right]}_{\mathcal{X}} \tag{15}$$

The vector $\mathcal{Y}$ has $3n$ elements. The vector $\mathcal{X}$ has $3 + 2n$ elements. For the preceding system to be solvable, $\mathcal{H}$ must have full rank, and $3n \geq 3 + 2n \Rightarrow n \geq 3$. Thus, as long as the wind remains constant over a time window of $3T_s$ (or, alternatively, each LTV is at least $3T_s$ wide in time) and $\mathcal{H}$ is full rank, then the SADS problem is observable. As long as attitude changes, meaning that $\boldsymbol{\Psi}_k$ are not constant, then $\mathcal{H}$ will have full rank. However, a simple "yes" or "no" on observability does not tell us anything about the quality (accuracy) of the estimates. What we want to know is how much do attitude and airspeed have to change to get an accurate estimate? To answer this question, we will look at the observability Gramian.

B. Maneuver Optimization Problem

To proceed with this analysis, we assume that sufficient time has elapsed, and the INS/GPS solution has converged such that the attitude errors are small. This means that C_n^b is known. The Gramian $\mathcal{G}_d$ over $l \cdot T_s$ is calculated to be using the discrete observability Gramian definition [Eq. (6) in [7]]:

$$\mathcal{G}_d = \mathcal{H}^T \mathcal{H} \tag{16}$$

As mentioned earlier, at least three different time steps are needed to achieve a rank of 5. However, if attitude and airspeed are not changed sufficiently over $3T_s$, then the matrix $\mathcal{H}$ of Eq. (15) may be ill-conditioned. If α and β are changing rapidly and significantly, then an even larger change in attitude and airspeed are required. We will start with a benign but unrealistic case of α and β being constant. This will provide a floor or the minimum attitude change required. We will relax this assumption later. Now, with the constant α and β assumption, Eq. (15) has dimensions of $3k \times 5$, and matrix $\mathcal{H}$ has the following form:

$$\mathcal{H}_c = \begin{bmatrix} \boldsymbol{\Psi}_1 & \boldsymbol{\Omega}_1 \\ \vdots & \vdots \\ \boldsymbol{\Psi}_k & \boldsymbol{\Omega}_k \\ \vdots & \vdots \\ \boldsymbol{\Psi}_n & \boldsymbol{\Omega}_n \end{bmatrix} \tag{17}$$

Hence, for a fixed time horizon T, the following Gramian is obtained:

$$\mathcal{G}_d = \mathcal{H}^T \mathcal{H} \text{ for nonconstant } \alpha \text{ and } \beta \tag{18}$$

$$= (\mathcal{H}_c)^T \mathcal{H}_c \text{ for constant } \alpha \text{ and } \beta \tag{19}$$

Krener and Ide [31] introduced measures of observability based on the condition number or the smallest singular value of the local observability Gramian. The condition number measures the degree of attenuation information experiences while traveling along the path from the measurements to the states. The larger the condition number, the more attenuated the information. The local observability Gramian can be calculated in the closed form in this case, and we will use this metric to quantify observability. Formally, measuring the degree of observability for the system can be formulated as the following optimization problem for the condition number of the observability Gramian $\kappa(\mathcal{G}_d)$, given next:

$$\begin{aligned} \underset{\boldsymbol{\psi}_{nb_1}, \ldots, \boldsymbol{\psi}_{nb_k}, \ldots, V_{a_1}, \ldots, V_{a_k}}{\operatorname{argmin}} \quad & \kappa(\mathcal{G}_d) \\ \text{s.t.} \quad & V_{a_{\min}} \leq V_a \leq V_{a_{\max}} \\ & \theta_{\min} \leq \theta \leq \theta_{\max} \\ & \phi_{\min} \leq \phi \leq \phi_{\max} \\ & \psi_{\min} \leq \psi \leq \psi_{\max} \end{aligned} \tag{20}$$

where $\boldsymbol{\psi}_{nb_k} = [\psi \quad \theta \quad \phi]^T$ and V_{a_k} are the set of Euler angles and airspeed at time step k. There are four linear constraints that represent, in part, the flight envelope of the aircraft. The goal is to minimize the condition number over a finite time horizon. Theoretically, the minimum condition number that can be obtained is 1, which is an indication that the given matrix is well conditioned and the states are well observed. The Gramian $\mathcal{G}_d$ for the constant α and β can become ill-conditioned due to the nature of the $\mathcal{H}_c$ matrix. The first three columns consist of the coordinate transformation matrix (with the norm equal to 1), but the last two columns are scaled by the airspeed (typically in the range of 15–25 m/s for small UAVs). This makes the entire matrix ill-conditioned. Therefore, the minimum acceptable condition number is a function of a particular aircraft's flight envelope. The minimum acceptable $\kappa_{\min}$ can be derived from the design requirements from users of the SADS. The definition of condition number of a matrix $\mathcal{G}_d$, denoted $\kappa(\mathcal{G}_d)$, is defined as

$$\kappa(\mathcal{G}_d) = \|\mathcal{G}_d\| \cdot \|\mathcal{G}_d{}^{-1}\| \tag{21}$$

where $\| \|$ is either the 2-norm or Frobenius norm of the Gramian [40]. Because the optimization problem in Eq. (20) is nonconvex (multiplication of sinusoidal functions), numerically solving it would not give us any meaningful insight (multiple local minimum solutions). Therefore, it is parsed into several suboptimization problems that are physically sound for practical aircraft maneuvers.

C. Two-Dimensional Versus Three-Dimensional Maneuver

As a concrete demonstration of how the insight gained from the observability analysis in the previous section can be used in affecting the performance of the SADS estimates, we exercise the estimator on a catalog of aircraft trajectories. A catalog of typical two-dimensional (2-D) and 3-D flight maneuvers is provided in Table 1. The double dashed lines in Table 1 mean that the variable is not being actively commanded; it only varies passively due to the coupled longitudinal and lateral motions. For example, if the heading angle is changing, then the roll angle will inevitably change. However, the roll angle can

Table 1 2-D and 3-D flight maneuver motion

Maneuver	V_a	ψ	θ	ϕ
		2-D case		
1	Constant	Constant	Varying	——
2	Constant	Varying	Constant	——
3	Constant	Constant	——	Varying
4	Varying	Constant	Varying	——
5	Varying	Varying	Constant	——
6	Varying	Constant	——	Varying
		3-D case		
1	Constant	Varying	Varying	——
2	Varying	Varying	Varying	——
3	Varying	Varying	Varying	Varying

return to zero while the heading remains at a new commanded value after the maneuver. We will consider the first 3-D case in Table 1 in detail to demonstrate the conditional observability analysis. All other cases can be analyzed in the same fashion. Some key results for this analysis are summarized at the end of this section.

D. Three-Dimensional Case Study Example

At least three different points in state space (i.e., $k = 1, 2, 3$) are needed for the Gramian $\mathcal{G}_d$ to achieve full rank. For the first case of 3-D motion, the $\mathcal{H}_c(1{:}3)$ matrix is used in the construction of $\mathcal{G}_d$ using Eq. (19). Because an aircraft can start from any orientation, the easiest orientation is picked as the reference point, which is to set all Euler angles to be 0 deg. The airspeed is set to be 15 m/s. For the second and third points in state space, ϕ is held to be the same angle, but ψ and θ are varied, giving the following $\mathcal{H}_c(1{:}3)$:

$$\mathcal{H}_c(1{:}3) = \begin{bmatrix} C_n^b(0,0,0\ \text{deg}) & \mathbf{\Omega}(V_a) \\ C_n^b\left(0\ \text{deg}, \frac{\theta_i}{2}, \frac{\psi_i}{2}\right) & \mathbf{\Omega}(V_a+\epsilon) \\ C_n^b(0\ \text{deg}, \theta_i, \psi_i) & \mathbf{\Omega}(V_a+\epsilon) \end{bmatrix} \tag{22}$$

where $\theta_i \in (-30, 30\ \text{deg})$, and $\psi_i \in (0, 180\ \text{deg})$. θ and ψ in the second row block of Eq. (22) are half of the values in the third row block. This is done to prevent a poor condition number. Also, small ϵ is necessary to prevent a poor condition number, and it is set to be 1 m/s. With $\mathcal{H}_c(1{:}3)$ covering all possible pitch and heading angles, Figs. 2 and 3a are obtained by calculating the 2-norm and F-norm condition number over a sweep of ψ and θ, respectively.

Figure 2 is the normalized 2-norm condition number for various ψ and θ. The normalized condition number is calculated by dividing every condition number by the minimum condition number. Figure 2 gives a guideline on how an airplane should maneuver to achieve a high degree of observability. For example, in Fig. 2, the red dot O represents the reference orientation $(\psi, \theta, \phi) = (0, 0, 0\ \text{deg})$, which is the initial of orientation of the aircraft. Now, suppose that the red dot A represents the final orientation [e.g., $(90, -20,\ 0\ \text{deg})$] of the aircraft in one flight maneuver sequence. A certain normalized condition number is achieved by this maneuver sequence from the initial orientation represented at O to the final orientation presented at A. The lower the condition number is, the higher degree of observability is achieved by the maneuver sequence.

Figure 3a is the normalized F-norm condition number for various ψ and θ. As can be seen in the figure, the dynamic range of the F-norm as a function of ψ and θ is larger than that for the 2-norm. For example, once the orientation deviates from point O, the condition number is immediately reduced to a flat region. The condition number is not further reduced if heading ψ and pitch angle θ are not changed together significantly. As such, the F-norm is a more sensitive indicator in the relationship between observability and aircraft maneuver aggressiveness.

Of course, this is a very optimistic analysis because α and β were assumed to be constant. When α and β are allowed to vary and $\mathcal{H}$ [Eq. (15)] is used to form the observability Gramian, Fig. 3b results. Figure 3b is effectively Fig. 3a with a "crown" of the surface removed. In other words, if α and β are changing, more aggressive attitude changes are needed to achieve a good degree of observability.

A similar analysis was carried out for the different cases listed in Table 1, and a summary of the key findings of this analysis follows.

1) Condition number does not improve significantly if heading angle stays at the reference value, regardless of how the pitch angle is changed. The same can be said if the pitch angle stays at the reference value while the heading angle is changed.

2) The minimum condition number is achieved by changing the aircraft's pitch and heading angle simultaneously (greatest gradient direction) as much as possible.

3) If the reference point is at (0, 0, 0 deg), then the figure is symmetric with respect to $\psi - \kappa_i$ or $\theta - \kappa_i$ (where $i = 2$ or F) planes. In other words, pitching down or up and changing heading

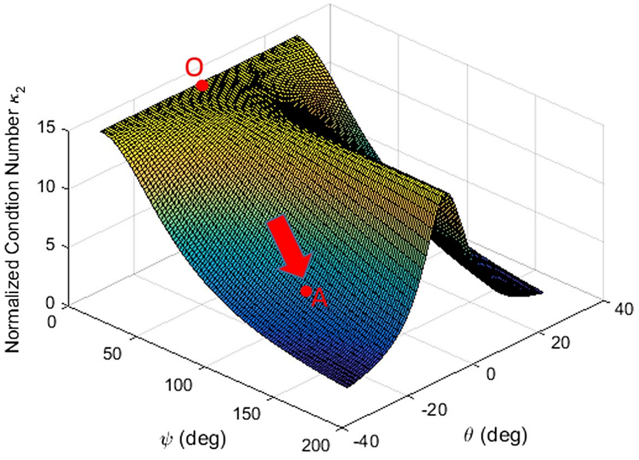

Fig. 2 Normalized 2-norm condition number over ψ and θ.

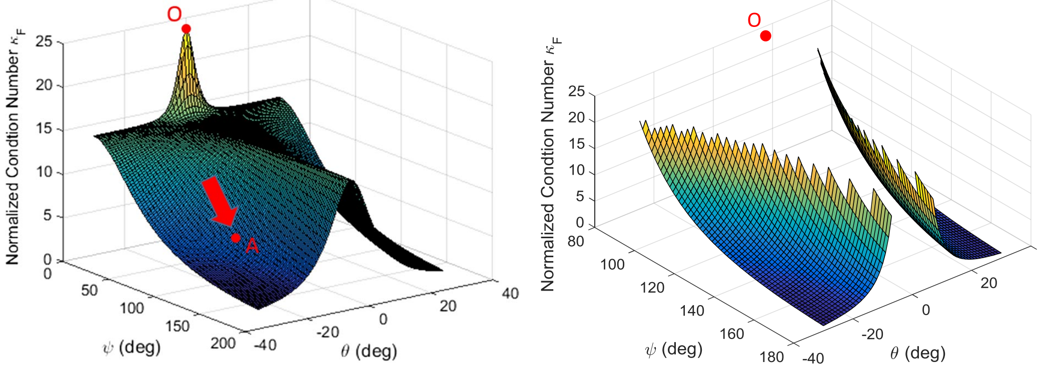

a) Normalized F-norm condition number over ψ and θ assuming α and β are constant over each LTV_K

b) Normalized F-norm condition number over ψ and θ assuming α and β changing over each LTV_K

Fig. 3 Normalized F-norm condition number over ψ and θ.

clockwise and counterclockwise have the same effect on condition number.

4) Varying airspeed while changing the orientation of the aircraft is the best flight maneuver to improve the condition number.

The observability analysis presented here is independent of the aircraft. The analysis can be applied to any aircraft to study observability. Furthermore, the analysis is not derived based on the typical flight trajectories such as a circular or a climb/descent trajectory. Instead, the flight trajectory is decomposed into points of the state space that we will refer to as the maneuver frame in this paper. Each maneuver frame is defined by the aircraft's orientation and airspeed. A sequence of maneuver frames forms a flight trajectory. The condition number of an LTV observability Gramian is used as a measure of observability, and its variation as a function of flight trajectory is examined to show how an aircraft can maneuver to achieve a high degree of observability.

E. Time Aspect of Maneuverability

The time it takes to maneuver from point O to point A shown in Figs. 2 and 3a is aircraft-dependent. For example, it might take a slightly longer time for a larger aircraft to maneuver from point O to point A than it would for a smaller, more agile aircraft. As we will discuss next, the length of the time interval required to go from one maneuver frame to the next and how the wind varies during this time interval have an important bearing on the SADS estimator observability.

1. Maneuver Frame Versus Estimator Rate

Recall that the maneuver frame is defined as one snapshot of the aircraft maneuver in the inertial coordinates, characterized by aircraft's orientation and airspeed. The rate at which an aircraft moves from one maneuver frame to the next depends primarily on the aircraft's dynamics. The estimator rate, defined as the rate at which the SADS estimator computes the air data states, is related to the sensor sampling rate. It is the rate at which the underlying nonlinear equations are linearized to form the LTV system used by the EKF. In Fig. 4, the flow of maneuver frames and its relationship to estimator rate are shown graphically. If the wind velocity vector is constant, then all that is required for observability is that the aircraft go from maneuver frame O to maneuver frame A. The number of sampling frames that elapse during the movement from O to A would be immaterial. However, the fact that the wind velocity vector is not a constant puts an upper bound on how slowly the aircraft can move from maneuver frame O to A and still maintain observability of the SADS estimator.

2. Wind Variation During Maneuvers

Figure 5 is a sectional cut at $\psi = 90$ deg of Fig. 2. Let τ_M the be maneuvering time from point O to any other maneuver frame (i.e., A, B, C, or D). Let τ_W be the time constant of the wind, the average time of wind variation. Let τ_M^U be the upper bound of the maneuvering time and τ_W^L be the lower bound of the time constant of the wind. The following inequality has to be satisfied to have an observable system:

$$\tau_M \leq \tau_M^U \leq \tau_W^L \leq \tau_W \tag{23}$$

Equation (23) states that maneuver time has to be less than the wind time constant. This supports the assumption of slow-varying wind. If an aircraft can maneuver fast enough and provide enough excitation before the wind changes, then the estimator is observable; the wind, angle of attack, and angle of sideslip can be estimated.

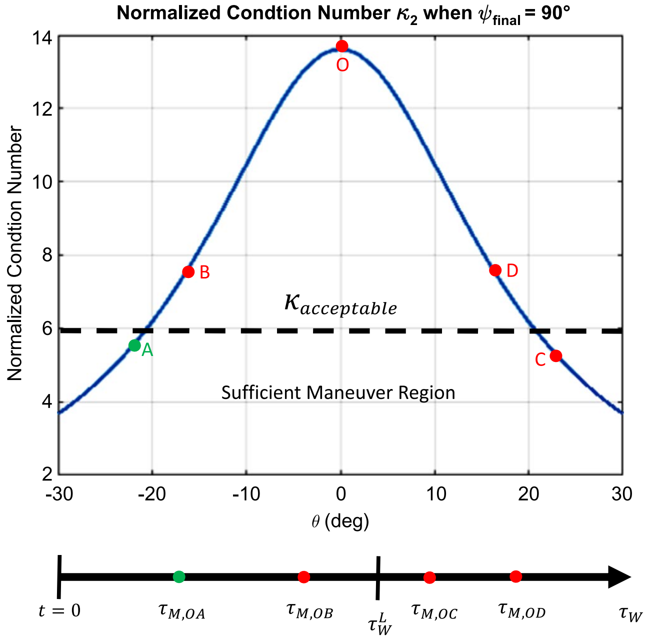

Fig. 5 Sectional cut of Fig. 2 when $\psi_{\text{final}} = 90$ deg.

This concept is depicted graphically in Fig. 5, which shows four hypothetical trajectories in the maneuver space: OA, OB, OC, and OD. It also shows a timeline of maneuver times. For the estimator to be observable, the maneuver has to satisfy two criteria; it must have achieved an acceptable condition number, and the maneuver time τ_M has to be less than the lower bound of wind time constant τ_W^L. Assuming that the area below the dotted line, denoted as the sufficient maneuver region, is the region of acceptable condition numbers, then OA and OC have an acceptable condition number, whereas OB and OD do not. For the maneuver time τ_M, it can be seen that $\tau_{M,\text{OA}}$ and $\tau_{M,\text{OB}}$ are less than τ_W^L, whereas $\tau_{M,\text{OC}}$ and $\tau_{M,\text{OD}}$ are not. Thus, as summarized in Table 2, the trajectory from O to A is observable.

The wind time constant depends on the weather condition on a given day. There are models for the variation of τ_W. For example, the work in [37] provides a model with an upper bound for τ_W, which is approximately 400 s.

V. Validation and Simulation Study

A. Simulation Setup

A modified version of the nonlinear aircraft Simulink model described in [41,42] is used for the simulation analysis that is discussed next. The parameters of the aircraft in the Simulink model are for an Ultra Stick 120 UAV, whose equations of motion were developed in [43]. Different maneuver sequences are simulated to test the observability analysis. For the sake of brevity, only case 2 of the 3-D cases listed in Table 1 is discussed here. Note that case 2 is a more generalized version of case 1 shown in Sec. IV.D. The airspeed in case 2 is varied to help increase the degree of observability through more vertical excitations. Case 2 consists of two maneuver sequences

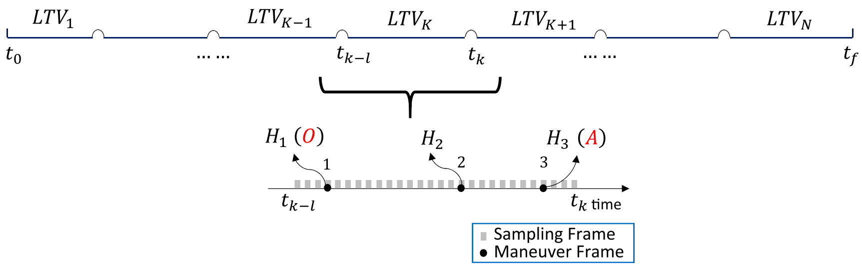

Fig. 4 Graphical depiction of the maneuver frame and sampling frame.

Table 2 Observability cases study based on normalized condition number $\kappa_{\text{acceptable}}$ and maneuver time τ_M

Case	$\kappa_{(\cdot)} < \kappa_{\text{acceptable}}$	$\tau_{M,(\cdot)} < \tau_W^L$	Observable maneuver?
OA	Yes	Yes	Yes
OB	No	Yes	No
OC	Yes	No	No
OD	No	No	No

(denoted maneuvers 1 and 2 in Table 1) executed sequentially. The wind direction is simulated to slowly vary horizontally from 30°W to 45°E in the first 75 s. The wind direction then is kept at 45°E. The downward wind is initially at $0.5\ \mathrm{m/s}$ and is then stepped to $-0.5\ \mathrm{m/s}$ at 150 s. The actuator noise is set to be zero for simplicity. The details of the maneuver and wind conditions can be found in Table 3. The measurement noise and the wind parameters of the simulation are listed in Table 4. The GPS and IMU parameters are chosen based on a consumer-level GPS and IMU [36]. The measurement error for airspeed is set to be 10% of the airspeed. This is determined to be sufficient to cover observed errors in the pitot tube based on the real flight calibration results.

To estimate the changes in the wind accurately during flight, a high degree of observability needs to be achieved. Varying heading constantly and sinusoidally varying airspeed (which leads to varying pitch angle) simultaneously is sufficient to accurately estimate the changes in the horizontal wind direction (maneuver 1 in Table 3). The rate of heading change and airspeed have to be faster than the rate of the horizontal wind directional change.

Table 3 3-D case 2 simulation description

Name	Time, s	Description
Maneuver 1	0–75	Steady flight with varying heading ψ constantly (in a figure-of-eight pattern); sinusoidally varying airspeed V_a ($\pm 4.5\ \mathrm{m/s}$ from average)
Maneuver 2	75–300	Aggressive flight with varying heading ψ constantly (in a figure-of-eight pattern); sinusoidally varying airspeed V_a ($\pm 8\ \mathrm{m/s}$ from average)
Wind condition 1	0–75	Start blowing from 30° W, then direction is slowly changing to 45° E in 75 s; downward wind: $0.5\ \mathrm{m/s}$
Wind condition 2	75–150	Stays at 45° E; downward wind: $0.5\,\mathrm{m/s}$ ($W_N = -3.5535\ \mathrm{m/s}$, $W_E = -3.5535\ \mathrm{m/s}$, $W_N = 0.5\ \mathrm{m/s}$)
Wind condition 3	150–300	Stays at 45° WE; downward wind: $-0.5\ \mathrm{m/s}$ ($W_N = -3.5535\ \mathrm{m/s}$, $W_E = -3.5535\ \mathrm{m/s}$, $W_N = -0.5\ \mathrm{m/s}$)
Miscellaneous	0–300	Actuator noise off

Maneuver 2 contains several pitch and altitude changes. These are required to make the vertical component of wind W_D observable. In addition to constant heading change, maneuver 2 also features large airspeed changes. This is done by commanding the aircraft to climb and descend at the maximum rate supported by the air frame and power plant (changes around $\Delta 8\ \mathrm{m/s}$). Figure 6a shows the trajectory of the simulated flight. The color bar represents the magnitude of the altitude. Figure 6b shows the simulated time history of airspeed, altitude, and throttle. Observe the large altitude variation (45–120 m) and concomitant large vertical velocity excitation of maneuver 2.

Figure 7 sheds light on why maneuver 2 is necessary for all the wind components to be observable. To estimate the 3-D wind vector, the aircraft must fly with a sufficient amount of different inertial velocities, particularly with large directional variations. This is shown on the left side of Fig. 7, where the inertial velocity vectors (green color vectors) are used to estimate the 3-D wind vector (the blue color vector). The aircraft can achieve sufficient variation in inertial velocity, particularly in the vertical direction, by flying through p_1, p_2, and p_3.

The right side of Fig. 7 illustrates how the flight trajectory points p_1, p_2, and p_3 can be thought of geometrically as a problem of estimating the radius and center of the sphere. If we translate the wind vector and all the inertial velocity vectors to the origin of the NED frame, the difference between the wind vector and inertial velocity vector is the airspeed vector (red vector). The inertial velocity vectors point to the surface of the sphere. When there are sufficient inertial velocity vectors, the center and radius of the sphere can be estimated. The radius of the sphere represents the airspeed magnitude. The center of the sphere is used in the wind triangle equation to obtain the 3-D wind vector. The yellow ellipsoid only represents partial wind observability space if the downward direction is not fully swept by the inertial velocity vector. In other words, the yellow ellipsoid is deficient for the 3-D wind estimation. Furthermore, inaccurate spherical estimation can also result in ambiguity in estimating the direction of the downward wind. This indicates that maneuvers containing large variations in pitch, altitude, and heading are needed to estimate the 3-D wind vector.

Maneuver 1 is not sufficient enough to capture the change in the downward wind. The vertical inertial velocity component V_D has to be the same order of magnitude as the horizontal inertial velocity components V_N and V_E to detect the downward wind change. Therefore, maneuver 2 is employed to provide both horizontal and vertical velocity excitations in the second phase of the flight simulation.

B. Simulation Results

Figure 8 shows the attitude estimates, attitude estimation error, and its $3-\sigma$ covariance bound for the entire flight. The uncertainty represented by $3-\sigma$ bound of the attitude decreases significantly at 75 s due to the longitudinal maneuver. The $3-\sigma$ bounds stop decreasing further and become oscillatory, especially in ψ. In real flight, the uncertainty bound for attitude should decrease further; the maneuvers

Table 4 Measurement and wind parameters setting for simulation

Parameter	Source	Variable	Simulation setting
Position	GPS position measurement	P_N, P_E, P_D	$\sigma_{P_D} = \sigma_{P_E} = \sigma_{P_D} = 3\ \mathrm{m}$
NED velocity	GPS velocity measurement	V_N, V_E, V_D	$\sigma_{V_N} = \sigma_{V_E} = \sigma_{V_D} = 0.2\ \mathrm{m/s}$
Airspeed	Pitot tube	V_a	$\sigma_{V_a} = 10\%\overline{V_a}$
Acceleration	IMU measurement	a_x, a_y, a_z	$\sigma_{\text{aw}} = 0.05\ \mathrm{m/s^2}$ $\sigma_{\text{ad}} = 5^{-3}\ g$ $\tau_a = 300\ \mathrm{s}$
Angular rate	IMU measurement	p, q, r	$\sigma_{\text{gw}} = 0.1\ \mathrm{deg/s}$ $\sigma_{\text{gd}} = 360\ \mathrm{deg/h}$ $\tau_g = 300\ \mathrm{s}$
Wind	Wind parameter	W_N, W_E, W_D	$\sigma_{W_N} = \sigma_{W_E} = 0.5\ \mathrm{m/s}$ $\sigma_{W_D} = 2.0\ \mathrm{m/s}$ $\tau_{W_N} = \tau_{W_E} = 1\ \mathrm{s}$ $\tau_{W_D} = 10\ \mathrm{s}$

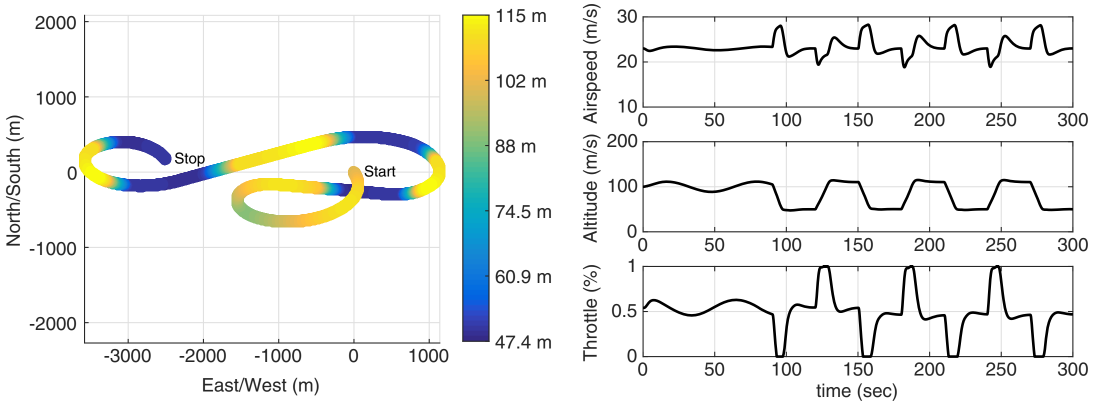

a) Simulated trajectory

b) Airspeed, altitude, and throttle setting time history. The vertical bar on the right provides a color code for altitude changes

Fig. 6 Simulated trajectory, airspeed, altitude, and throttle setting.

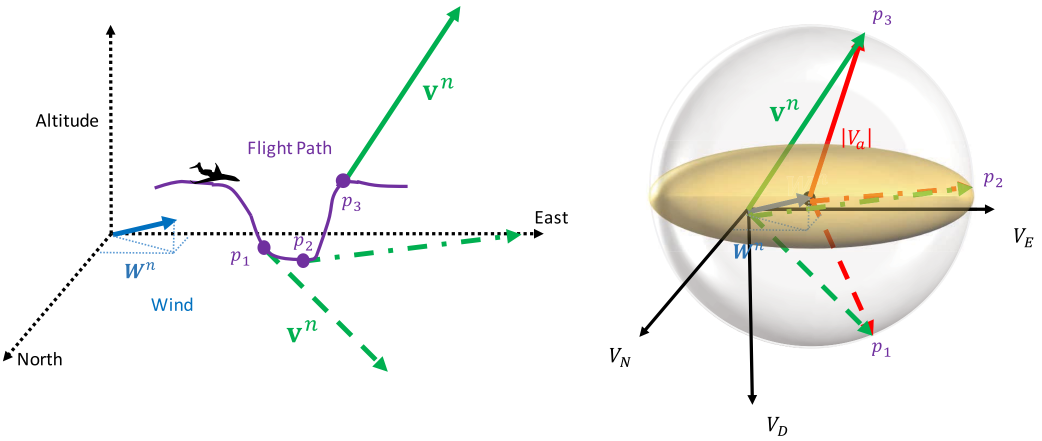

Fig. 7 Wind velocity estimation illustrated using sphere estimation.

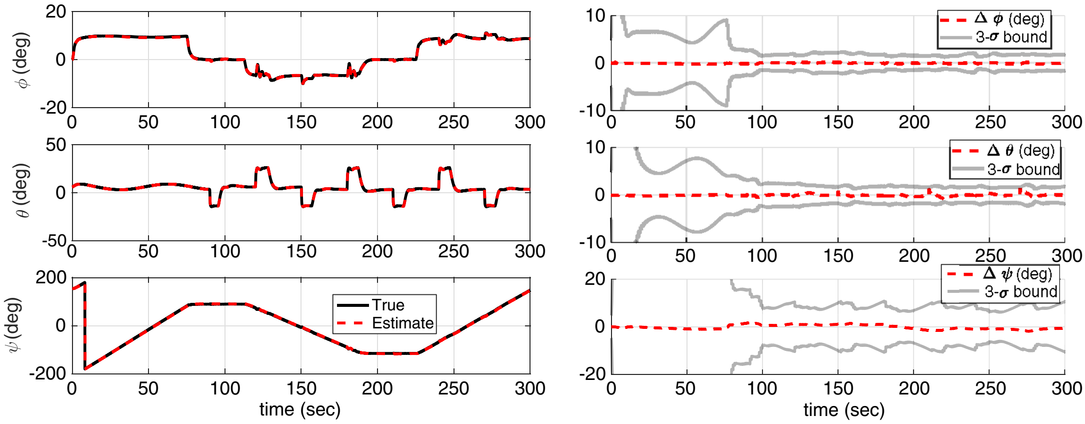

a) Euler angle time history

b) Euler angle error and its 3-σ bound

Fig. 8 Euler angle true and estimates and its $3-\sigma$ bounds.

will be more aggressive (e.g., include sharp turn) than the ones simulated.

Figure 9 shows the 3-D wind components, α, and β estimates. All the wind components converge to the true value after a sufficient amount of time and excitation. For the W_N and W_E components, the estimates slowly converge to the true value, whereas the magnitude of wind is changing over the first 75 s. The downward wind estimate W_D captures the vertical wind speed change at $t = 150$ s. The α estimate converged after about 20 s. When the downward wind changed direction at 150 s, the α estimate quickly converged to the true value. On the other hand, β estimate did not converge quickly to the true value. Stable convergence was achieved at $t = 210$ s. The accuracy of the attitude is critical to β estimation. For example, this can be observed by looking at the shape of the $3-\sigma$ bound for the β estimates shown in Fig. 9b; it mirrors the shape of the $3-\sigma$ bound of ψ.

The $1-\sigma$ of α and β estimate are determined to be 5.04 and 3.70 deg, respectively. The uncertainty of α and β is large and would

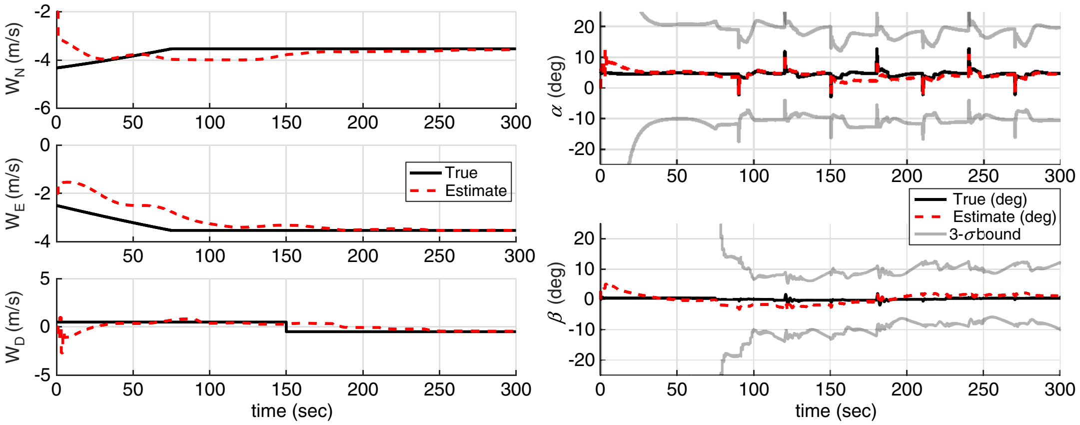

a) Simulated vs. estimated wind vector **b) Simulated vs. estimated α and β**

Fig. 9 Wind vector (true and estimates), α, β (true and estimates), and its $3-\sigma$ bounds.

generally be unacceptable. Note that the model-aided SADS estimator described in [1,3] reported a $3-\sigma$ covariance bound for the airspeed, angle of attack, and sideslip of 2 m/s, 3 deg, and 5 deg, respectively. The fact that the estimator proposed here is less accurate should not come as a surprise. After all, it is a model-free estimator and cannot leverage of information available from an aerodynamic model of the airplane. The following section explores the limitations of the estimates through sensitivity and error analysis. This analysis will give insight into how to improve the quality of the SADS estimates.

VI. Accuracy Limitation

The simulation of the previous section showed that the uncertainty of α and β can be rather large. In this section, we show how various factors affect the accuracy of α and β and why the minimum expected accuracy of α and β is mainly a function of the wind uncertainty and airspeed. The variance on the estimation errors of α and β [the diagonal entries of $\boldsymbol{P}_{\alpha\beta}$ in Eq. (8)] are given by

$$\boldsymbol{P}_{\alpha\beta}(1,1)=\sigma_\alpha^2=\underbrace{\left(\frac{\partial\alpha}{\partial V_N}\sigma_{V_N}\right)^2+\left(\frac{\partial\alpha}{\partial V_E}\sigma_{V_E}\right)^2+\left(\frac{\partial\alpha}{\partial V_D}\sigma_{V_D}\right)^2+\left(\frac{\partial\alpha}{\partial\phi}\sigma_\phi\right)^2+\left(\frac{\partial\alpha}{\partial\theta}\sigma_\theta\right)^2+\left(\frac{\partial\alpha}{\partial\psi}\sigma_\psi\right)^2}_{\text{INS/GPS}}$$
$$+\underbrace{\left(\frac{\partial\alpha}{\partial W_N}\sigma_{W_N}\right)^2+\left(\frac{\partial\alpha}{\partial W_E}\sigma_{W_E}\right)^2}_{\text{Horizontal Wind}}+\underbrace{\left(\frac{\partial\alpha}{\partial W_D}\sigma_{W_D}\right)^2}_{\text{Vertical Wind}} \tag{24}$$

$$\boldsymbol{P}_{\alpha\beta}(2,2)=\sigma_\beta^2=\underbrace{\left(\frac{\partial\beta}{\partial V_N}\sigma_{V_N}\right)^2+\left(\frac{\partial\beta}{\partial V_E}\sigma_{V_E}\right)^2+\left(\frac{\partial\beta}{\partial V_D}\sigma_{V_D}\right)^2+\left(\frac{\partial\beta}{\partial\phi}\sigma_\phi\right)^2+\left(\frac{\partial\beta}{\partial\theta}\sigma_\theta\right)^2+\left(\frac{\partial\beta}{\partial\psi}\sigma_\psi\right)^2}_{\text{INS/GPS}}$$
$$+\underbrace{\left(\frac{\partial\beta}{\partial W_N}\sigma_{W_N}\right)^2+\left(\frac{\partial\beta}{\partial W_E}\sigma_{W_E}\right)^2}_{\text{Horizontal Wind}}+\underbrace{\left(\frac{\partial\beta}{\partial W_D}\sigma_{W_D}\right)^2}_{\text{Vertical Wind}} \tag{25}$$

The off-diagonal terms of $\boldsymbol{P}_{\alpha\beta}$ representing correlations in the errors between the estimates of α and β are not discussed here. The key error sources are INS/GPS filter estimation errors and the uncertainty in the 3-D wind states. The $\sigma_{(\cdot)}$ in the first six terms of Eqs. (24) and (25) primarily represent the IMU errors and GPS measurement noise, and $\sigma_{W_{(\cdot)}}$ terms represent the wind modeling uncertainty.

Because all the derivatives and $\sigma_{(\cdot)}$ terms in both Eqs. (24) and (25) are time-varying, the time histories of the terms are examined. Figure 10 shows the error contributions of the three grouped terms in Eqs. (24) and (25) for σ_α and σ_β. The uncertainty of the downward wind estimate is seen to be the biggest uncertainty factor in σ_α and the smallest in σ_β. This points to one of the possible solutions for improving the accuracy of α and β: use higher-quality IMU and GPS sensors. In the following section, various IMU and GPS sensors are simulated to assess the impact on the accuracy of α and β.

A. Inertial Measurement Unit and Global Positioning System Contribution

The quality of the IMU and GPS measurement depend on the quality of the sensors. The output of each inertial sensor (gyro or accelerometer) of the IMU is modeled as an additive noise and bias. The additive noise is assumed to be wide-band noise with a given variance. The bias is assumed to be a first-order Gauss–Markov process, which is characterized by a variance and a time constant. For simplicity, we assume that all three accelerometers and all three gyros in the IMU are identical. Thus, a total of six parameters are required to model the IMU errors. For the GPS, an additive noise model is assumed in both position and velocity measurements. Thus, the impact on the accuracy of α and β can be examined by varying the error model parameters in a Monte Carlo analysis. Both IMU and GPS parameters and their possible ranges are listed in Table 5.

Figure 11 summarizes the key results from the Monte Carlo simulation conducted to assess how each parameter affects the accuracy of α and β. A starting point for these simulations is what we call the baseline filter. This is a filter whose sensor error

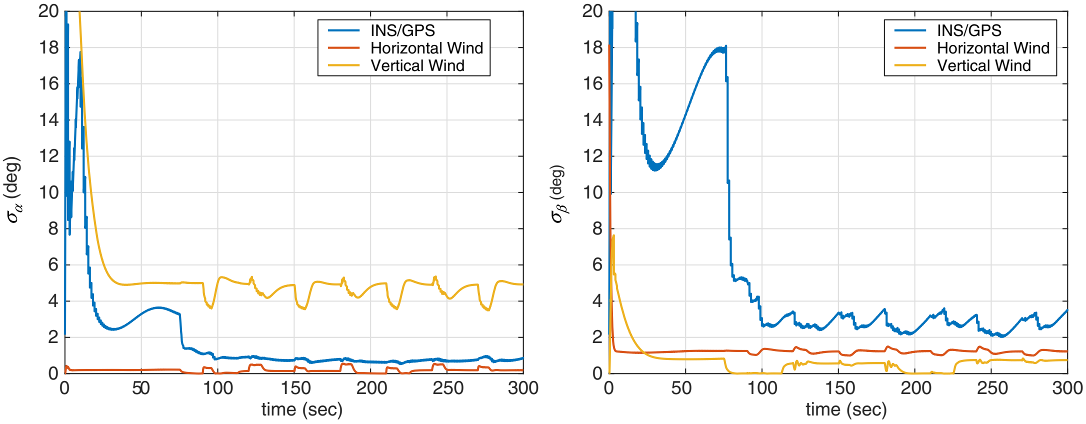

a) Various error contribution in σ_α **b) Various error contribution in σ_β**

Fig. 10 Various error contribution in σ_α and σ_β.

characteristics are given in Table 4. For each Monte Carlo run, a particular error parameter in the baseline filter is perturbed to assess the impact on the accuracy of the estimates of α and β. The process and measurement noise matrices are changed according to the assigned parameter in each run. For each set of parameters, 20 Monte Carlo simulations are conducted. The averages of the final steady-state values of σ_α and σ_β for all 20 runs are plotted against various parameters.

Figure 11a and 11b show how the gyro and accelerometer parameters affect the accuracy of α and β. In Fig. 11a, σ_α is insensitive to both σ_{gw} and σ_{aw}, whereas σ_β is more sensitive to σ_{aw} than σ_{gw}. In Fig. 11b, both σ_α and σ_β are insensitive to σ_{gd} and σ_{ad}. What these results show is that care has to be taken when choosing the correct parameters. For example, a better IMU does not necessarily improve accuracy much in terms of the σ of α and β.

Figures 11c and 11d show how GPS position and velocity noise affect the accuracy of α and β. In Fig. 11c, σ_α stays around 5 deg and occasionally exceeds 5 deg. The phenomenon is more apparent in σ_β. σ_β often jumps to abnormal values when σ_{P_D} is greater than 1 m. Overall, both α and β are much more sensitive to σ_{P_D} than $\sigma_{P_{NE}}$.

Figure 11d shows that α and β are more sensitive to σ_{V_D} than $\sigma_{V_{NE}}$ in terms of the σ value. Only a small range of $\sigma_{V_{(\cdot)}}$ is shown because anything greater than those values causes the σ values to become much worse or even diverge. Comparing the range of the GPS position and velocity used in this analysis, it is found that α and β are more sensitive to GPS velocity measurement error than GPS position measurement error. The effect of GPS is greater than the effect of IMU on the accuracy of α and β, and having a better GPS can reduce uncertainty significantly. Therefore, to obtain measurements sufficient to achieve the accuracy shown in this paper using the proposed estimator, a high-price-range consumer-grade GPS and a middle-price-range IMU are needed.

Table 5 INS/GPS sensor error model parameters for tradeoff study

Sensor	Variable	Range (tactical to consumer grade [36])
GPS	$\sigma_{P_D}, \sigma_{P_E}, \sigma_{P_D}$	0.01–10 m
	$\sigma_{V_N}, \sigma_{V_E}, \sigma_{V_D}$	0.01–1 m/s
Accelerometer	σ_{aw}	0.05–0.1 m/s^2
	σ_{ad}	$5\times10^{-6} - 5\times10^{-3}$ g
	τ_a	50–300 s
Rate gyro	σ_{gw}	0.01–5 deg/s
	σ_{gd}	0.005–1080 deg/h
	τ_g	50–300 s

B. Wind Limitation

The previous section has narrowed down how IMU and GPS affect the accuracy of α and β. In this section, the effect of wind parameters on the accuracy of α and β is examined. It is stated earlier that the largest error source that affects the variance of α is the wind parameters, and it is also the secondary error source contributing to the variance of β. Furthermore, the uncertainty σ_{W_D} is the biggest error source entering the estimator.

The wind is modeled by the first-order Gauss–Markov model, and the parameters are determined empirically. Ideally, the three components of the wind can be all equal to zero on a very calm day. However, there is usually a steady dominating horizontal wind. When this happens, the downward wind W_D (prevalent wind) is usually relatively small compared to the W_N and W_E components, and it is mainly dominated by wind gust and turbulence. To capture the downward wind in the presence of a dominating horizontal wind, the variance of the Markov process for the downward wind has to be larger than the variance of the Markov process for the horizontal wind. This relationship is shown in Eq. (26), where the variance of the downwind has to be greater than both of the variance of the north and east wind components, and it is empirically determined that the ratio of the variance between 1.5 and 10 works well:

$$\frac{2\sigma_{W_N}^2}{\tau_{W_N}} = \frac{2\sigma_{W_E}^2}{\tau_{W_E}} < \frac{2\sigma_{W_D}^2}{\tau_{W_D}} \tag{26a}$$

$$\frac{2\sigma_{W_D}^2/\tau_{W_D}}{2\sigma_{W_N}^2/\tau_{W_N}} \in (1.5, 10) \tag{26b}$$

The time constant τ_W reflects how fast the wind is changing over time. The maneuvering time τ_M has to be less than or equal to τ_W [Eq. (23)]. The UAV used in this paper has a time constant 0.14 s of the short-period mode, and the short-period mode reflects how fast the aircraft can quickly self-damp when the stick is briefly displaced. To satisfy Eq. (23), τ_{W_N} and τ_{W_E} are chosen to be 1 s. Similarly, the time constant of the phugoid mode is 9.53 s, and the phugoid is caused by a repeated exchange of airspeed and altitude. This relates to the vertical excitation in the downward wind direction; thus, τ_{W_D} is chosen to be 10 s. Although the analysis to determine parameters here is heuristic, more rigorous work can and should be done in the future.

With predetermined time constant τ_W, it is found that setting $\sigma_{W_N} = \sigma_{W_E} = 0.5$ m/s and $\sigma_{W_D} = 2$ m/s works well with both simulation and flight data when there is a dominating horizontal wind (3–6 m/s). If the flight is conducted in a very calm day, then the

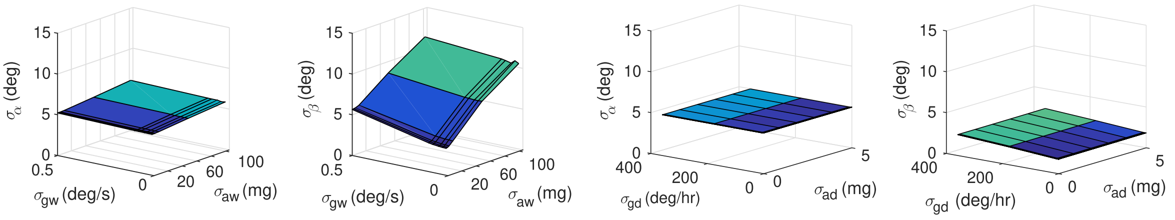

a) Sensitivity analysis with respect to σ_{aw} and σ_{gw} **b) Sensitivity analysis with respect to σ_{ad} and σ_{gd}**

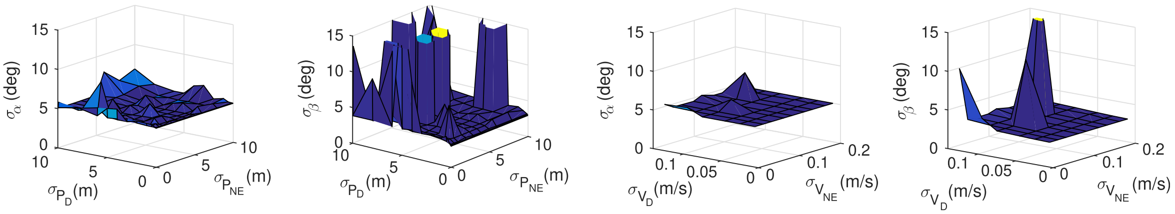

c) Sensitivity analysis with respect to $\sigma_{P_{NE}}$ and σ_{P_D} **d) Sensitivity analysis with respect to $\sigma_{V_{NE}}$ and σ_{V_D}**

Fig. 11 Sensitivity of α and β with various parameters in IMU and GPS.

performance of the estimator will be degraded because the wind condition does not match the presumed wind modeling parameter setting.

The estimator can be improved if the uncertainty in the wind is small. If there is an external sensor (e.g., accurate weather broadcast data) that can measure the 3-D wind with good accuracy, the accuracy of α and β can be improved. Improved wind models usually account for gust and turbulence, but it does not reduce the uncertainty in the wind. Therefore, for any synthetic air data estimation, the uncertainty in wind limits the accuracy of α and β.

C. Airspeed Limitation

For small UAVs, the airspeed is usually low and in the range of 12–30 m/s. The impact of airspeed on the SADS estimates can be determined by using the following error equations:

$$\delta\alpha = -\frac{w}{u^2+w^2}\delta u + \frac{u}{u^2+w^2}\delta w \tag{27}$$

$$\delta\beta = -\frac{uv}{V_a^2\sqrt{u^2+w^2}}\delta u + \frac{u^2+v^2}{V_a^2\sqrt{u^2+w^2}}\delta v - \frac{vw}{V_a^2\sqrt{u^2+w^2}}\delta w \tag{28}$$

If $u \gg v$ and $u \gg w$, Eqs. (27) and (28) can be further simplified as the following:

$$\delta\alpha \approx \frac{1}{u}\delta w = \delta\theta + \frac{1}{u}(\cos\theta\delta V_N - \cos\theta\delta W_N - \sin\theta\delta V_D + \sin\theta\delta W_D) \tag{29}$$

$$\begin{aligned}\delta\beta \approx \frac{1}{u}\delta v = -\delta\psi + \frac{1}{u}(&-\sin\psi\delta V_N + \sin\psi\delta W_N + \cos\psi\delta V_E\\ &-\cos\psi\delta W_E)\end{aligned} \tag{30}$$

From Eqs. (29) and (30), if the airspeed is large (represented by the u term), then the accuracy of α and β largely depends the accuracy of the attitude estimate. The uncertainty of inertial velocity and wind velocity are suppressed by the large airspeed. In other words, when the aircraft is operating at a high speed, the magnitude of the wind is much smaller than the airspeed, and so the wind uncertainty is relatively small.

By squaring each term in Eqs. (29) and (30), and assigning some typical values for $\delta V_{(\cdot)}$ and $\delta W_{(\cdot)}$ (the σ_W and σ_V values in Tables 4 and 5), and some reference point at $\theta = 5$ deg and $\psi = 0$ deg, the following trend shown in Fig. 12 is obtained for σ_α and σ_β. From Fig. 12, σ_α and σ_β are well below 1 deg when u is greater than 40 m/s, given an accurate σ_θ and σ_ψ (e.g., 0.5 deg) as an example.

Increasing airspeed would improve the accuracy of α and β if the attitude accuracy is reasonable. However, because small UAVs cannot usually operate over 25 m/s, σ_α and σ_β can only be reduced to some extent even if the attitude is relatively accurate.

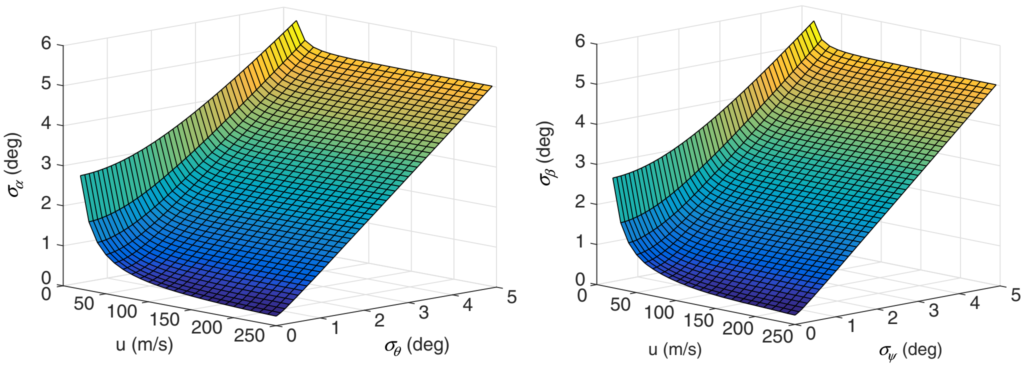

a) Effects of airspeed and attitude on the accuracy of σ_α **b) Effects of airspeed and attitude on the accuracy of σ_β**

Fig. 12 Effects of airspeed and attitude on the accuracy of σ_α and σ_β.

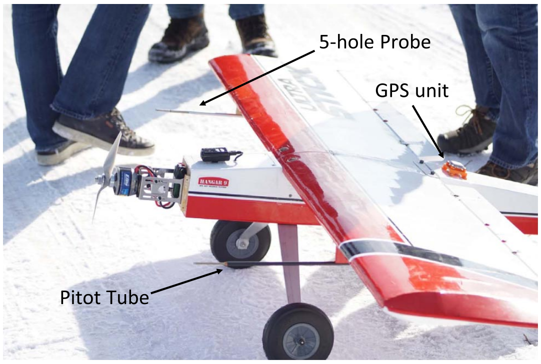

Fig. 13 Ultra Stick 120 setup.

VII. Flight Test

Experimental validation of the model-free synthetic air data estimator was accomplished by postprocessing the flight-test data collected using the UltraStick 120 testbed shown in Fig. 13. The goal of the flight test was to compare the performance of the estimator against the traditional air data system installed on the aircraft. The airframe is a low-cost fixed-wing radio-controlled aircraft with standard elevator, aileron, and rudder control surfaces. The physical and geometric properties can be found in [1]. The Ultra Stick 120 is equipped with a traditional pitot static system, a GPS receiver (u-blox-Neo-M8N), and an IMU (Invensense MPU-9250). These sensors are used to generate the α and β estimates. The ground truth for α and β is supplied by a five-hole probe [44,45]. A five-hole probe is a specially designed pitot tube that provides α, β, and V_a measurements. The five-hole probe is calibrated with wind-tunnel data initially and then calibrated in-situ to account for local flow conditions and alignment. In addition, an integrated INS/GPS system onboard provides position, inertial velocity, and attitude estimates.

Table 6 IMU and GPS sensor error model parameters for flight test

Sensor	Setting
GPS	$\sigma_{P_N} = \sigma_{P_E} = 3\ \mathrm{m}$, $\sigma_{P_D} = 6\ \mathrm{m}$ $\sigma_{V_N} = \sigma_{V_E} = 0.5\ \mathrm{m/s}$, $\sigma_{V_D} = 1\ \mathrm{m/s}$
Accelerometer	$\sigma_{\mathrm{aw}} = 0.05\ \mathrm{m/s^2}$ $\sigma_{\mathrm{ad}} = 0.01\ \mathrm{m/s^2}$ $\tau_a = 100\ \mathrm{s}$
Rate gyro	$\sigma_{\mathrm{gw}} = 0.00175\ \mathrm{rad/s}$ $\sigma_{\mathrm{gd}} = 0.00025\ \mathrm{rad/s}$ $T_g = 50\ \mathrm{s}$

The flight data used in this paper were collected on 21 June 2018. Although the main objective of the test was not solely for the air data estimation, the flight maneuvers were designed to provide sufficient excitation for the estimation. Wind circles, push-over–pull-up (±2 g), and rudder-induced steady forward slip maneuvers were conducted before other flight maneuver tests. The sensor error model parameters of IMU and GPS used for this flight test are given in Table 6. The wind parameters are the same as the one used in the simulation. The IMU runs at 50 Hz for the time update, whereas the GPS runs at 1 Hz for the measurement update.

Finally, to validate the wind estimation results, 3-D wind components are collected during the flight test by a remote anemometer located about 2.2 km away from the flight-test site. The anemometer is located at a height of 127.9 m, and its measurements are taken at 20 Hz. Although the measurements are not directly taken over the test field, it provides a reasonable check for the wind estimation, particularly in the wind direction.

Figures 14 and 15 show a portion of the flight-test results. Figure 14 shows the 3-D wind estimates and the mean of the wind measurements taken by the remote anemometer. The three standard deviations of the wind components are also calculated and plotted in Fig. 14. The magnitude of these estimates are very similar to the mean values. They are also within the three standard deviations. From Figs. 15a and 15b, it can be seen that the α estimate is reasonably good compared to the five-hole calibrated α measurement, and the estimate generally stays within the $3-\sigma$ bound. On the other hand, the β estimate momentarily goes out of the $3-\sigma$ bound right after a sharp turn at $t \approx 1275$ s. This sharp turn is manifested by the significant change in ϕ from a wing-level condition where β stays constant at about −5 deg. This is due to INS/GPS attitude estimation errors. To further analyze why the estimate is biased in this turn as well as to understand the behavior of the $3-\sigma$ bound of α and β, another

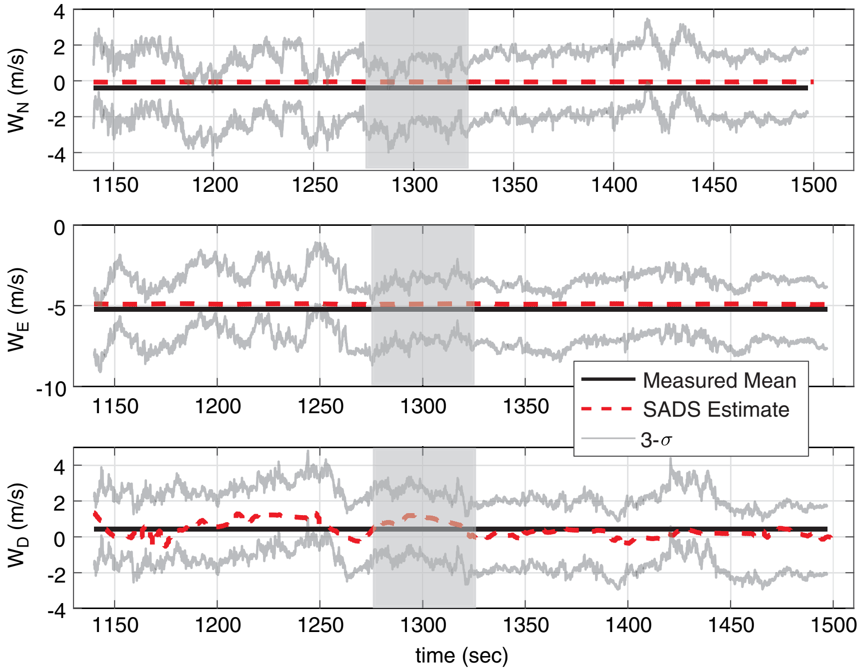

Fig. 14 Flight-test results: 3-D wind estimates.

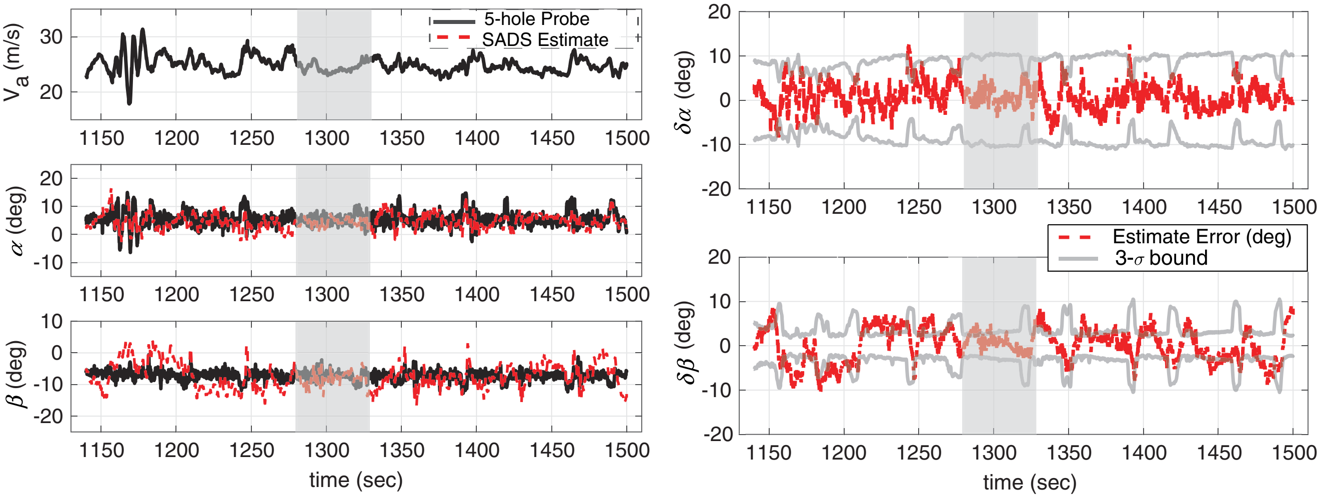

a) Flight test airspeed measurement and α and β estimates b) Flight test α and β estimate error and its $3-\sigma$ bound

Fig. 15 Flight-test results: α and β.

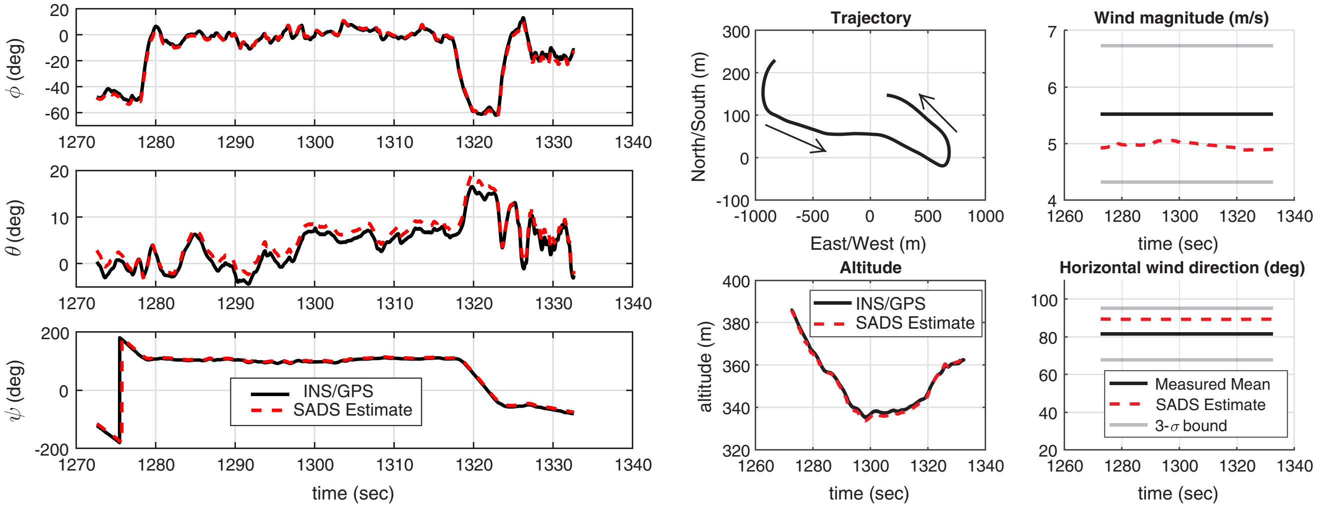

a) Highlighted flight test euler angle INS/GPS Nav solution vs. estimates b) Highlighted flight test trajectory, altitude, wind estimates

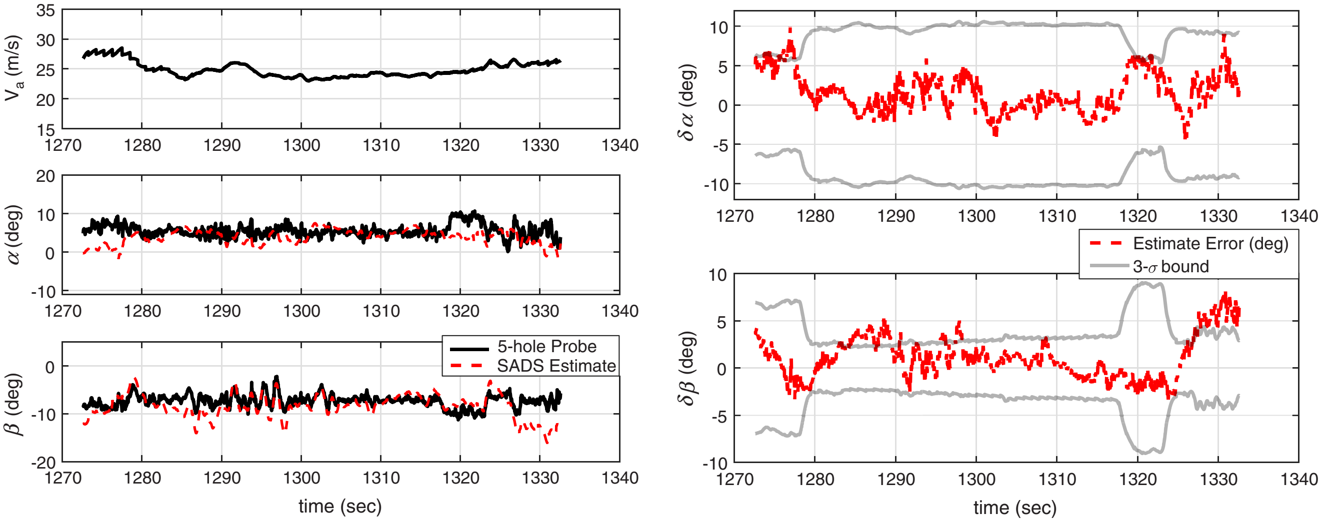

c) Highlighted flight test airspeed measurement and α and β estimates d) Highlighted flight test α and β estimate error

Fig. 16 Flight-test results of the highlighted gray region.

section of the flight-test results (around $t = 1300$ s and highlighted by the gray shading) is examined closely in Fig. 16.

The trajectory, altitude, wind magnitude, and direction estimates of the highlighted gray region are shown in Fig. 16b. The UAV just made a sharp turn before flying to the east direction. Then, the UAV was fighting against the wind before making another sharp turn back to the west direction. Figures 16c and 16d show the estimates, estimation errors, and $3-\sigma$ bound for α and β in the highlighted

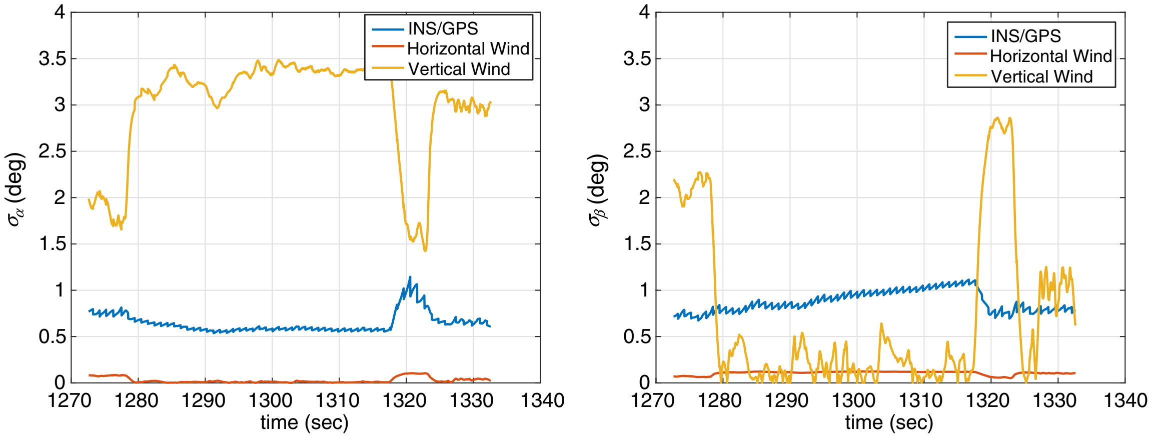

a) **Error contribution to σ_α during the grey flight test region**

b) **Error contribution to σ_β during the grey flight test region**

Fig. 17 Error contribution to σ_α and σ_β in the gray highlighted region of Figs. 15a and 15b.

region. The $1-\sigma$ bounds for α and β shown in Fig. 16d are determined to be 3.07 and 1.28 deg, respectively, which is a significant improvement compared to the simulation results, due to the more aggressive maneuver performed in the real flight test. The α estimate is reasonably accurate before the sharp turn. Interestingly, the β estimate seems to be accurate during the turn but starts going out of the bound after the turn. Although this maneuver can provide good excitation for the estimator, the maneuver itself is aggressive, which can result in poor estimates in attitude, inertial velocities, and wind estimates. This can be seen in the deviation in the θ estimate from the INS/GPS solution as well as the changes in wind estimates. Also, the uncertainties in all inertial velocity estimates increase during the sharp turns (not shown here), which leads to errors in α and β.

The poor estimates can also be explained by the various error contributions shown in Fig. 17. When the attitude maneuvers are benign ($1280 \leq t \leq 1320$ s), the biggest error contribution to α comes from the uncertainty in the vertical wind estimate, and the second largest contribution comes from the INS/GPS filter's attitude estimation errors. The smallest error in σ_α comes from the uncertainty in the horizontal wind estimate. When the sharp turn occurs ($t \approx 1320$ s), the error from the vertical wind estimate drops drastically because the sharp turn provides a sudden huge excitation in the downward direction, whereas the uncertainty in both INS/GPS and horizontal wind increase. The INS/GPS filter normally does not provide good estimates when there is a sudden dynamic change and sensor biases are not accurately estimated. This explains the increase in the INS/GPS error. The increase of the uncertainty in the horizontal wind estimate is also caused by the sudden directional change of the aircraft. All the error contributors of σ_α return to the nominal level when the aircraft finishes the sharp turn.

The error contributions in σ_β behavior is slightly different from the simulation shown previously in Fig. 10. The error of INS/GPS ramps up during a relatively straight flight and decreases during the sharp turn. This is expected because the heading state ψ of INS/GPS becomes less observable when there is no vehicle acceleration (e.g., turning flight). Once the turn is made, the degree of observability increases again. The error contribution from the vertical wind increases significantly when the sharp turn occurs. This signals that the error from the vertical wind does play a huge factor in the β accuracy. That is, the β estimate should not be relied on when the error contribution from the vertical wind exceeds the INS/GPS error contribution.

VIII. Conclusions

This paper presented a method for estimating 3-D wind vector, angle of attack, and angle of sideslip without the aerodynamic model of the aircraft. The observability analysis shows that the system is conditionally observable, provided that wind speed and direction do not change faster than the aircraft dynamics. A sensitivity analysis was performed to show what factors affect the accuracy of the angle of attack and sideslip estimates. Specifically, the variance of the downward wind is the largest limiting factor to the angle of attack and angle of sideslip estimations. A low airspeed would also decrease the accuracy due to the relative increasing wind effect on the aircraft. Furthermore, the accuracy of the attitude estimation also plays a significant role in estimating angle of attack and angle of sideslip. The conclusion of this is that an inexpensive, model-free air data estimator can still provide reasonably accurate estimate of α and β ($1-\sigma$ bound for a slow-flying unmanned aerial vehicle of approximately 5 and 3 deg, respectively) in the absence of an air data system and a dynamics model of the aircraft. The method and results presented in this paper suggest that a synthetic air data systems estimator can potentially be used as part of a fault detection and isolation scheme for traditional air data systems.

Appendix: Derivation of Flow Angle Covariance

To calculate all the components of $A_{\alpha\beta}$, recall that α and β can be calculated as

$$\alpha = \tan^{-1}\frac{w}{u}, \; \beta = \sin^{-1}\frac{v}{\sqrt{u^2+v^2+w^2}} \tag{A1}$$

Using the wind triangle kinematic relationship and Eq. (A1), all the components can be calculated as follows:

$$\begin{aligned} \frac{\partial\alpha}{\partial(\cdot)} &= \frac{\partial\alpha}{\partial u}\frac{\partial u}{\partial(\cdot)} + \frac{\partial\alpha}{\partial w}\frac{\partial w}{\partial(\cdot)} \\ \frac{\partial\beta}{\partial(\cdot)} &= \frac{\partial\beta}{\partial u}\frac{\partial u}{\partial(\cdot)} + \frac{\partial\beta}{\partial v}\frac{\partial v}{\partial(\cdot)} + \frac{\partial\beta}{\partial w}\frac{\partial w}{\partial(\cdot)} \end{aligned} \tag{A2}$$

where the partial derivative with respect to the position, accelerometer, and gyro biases is zero. For completion, all the partial derivatives involved are shown in Eqs. (A3) and (A4):

$$\begin{aligned} &\frac{\partial\alpha}{\partial u} = -\frac{w}{u^2+w^2} \quad \frac{\partial\alpha}{\partial v} = 0 \quad \frac{\partial\alpha}{\partial w} = \frac{u}{u^2+w^2} \\ &\frac{\partial\beta}{\partial u} = -\frac{uv}{V_a^2\sqrt{V_a^2-v^2}} \quad \frac{\partial\beta}{\partial v} = \frac{1-(v^2/V_a^2)}{\sqrt{V_a^2-v^2}} \quad \frac{\partial\beta}{\partial w} = -\frac{vw}{V_a^2\sqrt{V_a^2-v^2}} \end{aligned} \tag{A3}$$

$$
\begin{aligned}
&\frac{\partial u}{\partial V_N} = \cos\theta\cos\psi, \quad \frac{\partial u}{\partial V_E} = \cos\theta\sin\psi, \quad \frac{\partial u}{\partial V_D} = -\sin\theta, \quad \frac{\partial u}{\partial \phi} = 0\\
&\frac{\partial u}{\partial \theta} = -\sin\theta\cos\psi(V_N - W_N) - \sin\theta\sin\psi(V_E - W_E) - \cos\theta(V_D - W_D)\\
&\frac{\partial u}{\partial \psi} = -\cos\theta\sin\psi(V_N - W_N) + \cos\theta\cos\psi(V_E - W_E), \quad \frac{\partial u}{\partial W_N} = -\cos\theta\cos\psi, \quad \frac{\partial u}{\partial W_E} = -\cos\theta\sin\psi\\
&\frac{\partial u}{\partial W_D} = \sin\theta, \quad \frac{\partial v}{\partial V_N} = \sin\phi\sin\theta\cos\psi - \cos\phi\sin\psi, \quad \frac{\partial v}{\partial V_E} = \sin\phi\sin\theta\sin\psi - \cos\phi\cos\psi, \quad \frac{\partial v}{\partial V_D} = \sin\phi\cos\theta\\
&\frac{\partial v}{\partial \phi} = (\cos\phi\sin\theta\cos\psi + \sin\phi\sin\psi)(V_N - W_N) + (\cos\phi\sin\theta\sin\psi - \sin\phi\cos\psi)(V_E - W_E) + \cos\phi\cos\theta(V_D - W_D)\\
&\frac{\partial v}{\partial \theta} = (\sin\phi\cos\theta\cos\psi)(V_N - W_N) + \sin\phi\cos\theta\sin\psi(V_E - W_E) - \sin\phi\sin\theta(V_D - W_D)\\
&\frac{\partial v}{\partial \psi} = (-\sin\phi\sin\theta\sin\psi - \cos\phi\cos\psi)(V_N - W_N) + (\sin\phi\sin\theta\cos\psi - \cos\phi\sin\psi)(V_E - W_E)\\
&\frac{\partial v}{\partial W_N} = -(\sin\phi\sin\theta\cos\psi - \cos\phi\sin\psi), \quad \frac{\partial v}{\partial W_E} = -(\sin\phi\sin\theta\sin\psi - \cos\phi\cos\psi), \quad \frac{\partial v}{\partial W_D} = -\sin\phi\cos\theta\\
&\frac{\partial w}{\partial V_N} = \cos\phi\sin\theta\cos\psi + \sin\phi\sin\psi, \quad \frac{\partial w}{\partial V_E} = \cos\phi\sin\theta\sin\psi - \sin\phi\cos\psi, \quad \frac{\partial w}{\partial V_D} = \cos\phi\cos\theta\\
&\frac{\partial w}{\partial \phi} = (-\sin\phi\sin\theta\cos\psi + \cos\phi\sin\psi)(V_N - W_N) + (-\sin\phi\sin\theta\sin\psi - \cos\phi\cos\psi)(V_E - W_E) - \sin\phi\cos\theta(V_D - W_D)\\
&\frac{\partial w}{\partial \theta} = (\cos\phi\cos\theta\cos\psi)(V_N - W_N) + \cos\phi\cos\theta\sin\psi(V_E - W_E) - \cos\phi\sin\theta(V_D - W_D)\\
&\frac{\partial w}{\partial \psi} = (-\cos\phi\sin\theta\sin\psi + \sin\phi\cos\psi)(V_N - W_N) + (\cos\phi\sin\theta\cos\psi + \sin\phi\sin\psi)(V_E - W_E)\\
&\frac{\partial w}{\partial W_N} = -(\cos\phi\sin\theta\cos\psi + \sin\phi\sin\psi), \quad \frac{\partial w}{\partial W_E} = -(\cos\phi\sin\theta\sin\psi - \sin\phi\cos\psi), \quad \frac{\partial w}{\partial W_D} = -\cos\phi\cos\theta
\end{aligned}
\tag{A4}
$$

Acknowledgments

The authors gratefully acknowledge UTC Aerospace Systems in Burnsville, Minnesota, for donating the five-hole pitot tubes that are used in this work. The authors also acknowledge the Minnesota Invasive Terrestrial Plants Center for financial support to research issues associated with increasing the reliability of small UAV technology used for surveying applications. The flight data described in this paper are collected and conducted by University of Minnesota under contract to Systems Technology Inc. as part of a Phase II Small Business Innovation Research (SBIR) program for NASA Langley Research Center that is investing Unmanned Aerial System (UAS) handling qualities. The authors would also like to thank NASA (via grant NNX15AV67G), University of Minnesota–The Office of the Vice President for Research–Minnesota's Discovery, Research, and InnoVation Economy (UMN OVPR MnDRIVE) Initiative, Sentera LLC, and LMCCR Legislature of the State of Minnesota for supporting this work. Finally, the authors also gratefully acknowledge the help of Curtis Olson, member of the UAV lab, for conducting flight tests, and the University of Minnesota Eolos Wind Energy Research Group for the wind measurements. However, any opinions, findings, conclusions, or recommendations in this paper are those of the authors and do not necessarily reflect views of any of the preceding organizations.

References

[1] Lie, F. A. P., and Gebre-Egziabher, D., "Synthetic Air Data System," *Journal of Aircraft*, Vol. 50, No. 4, 2013, pp. 1234–1249. doi:10.2514/1.C032177

[2] Nebula, F., Palumbo, R., Morani, G., and Corraro, F., "Virtual Air Data System Architecture for Space Reentry Applications," *Journal of Spacecraft and Rockets*, Vol. 46, No. 4, 2009, pp. 818–828. doi:10.2514/1.42485

[3] Lie, F. A. P., and Gebre-Egziabher, D., "Sensitivity Analysis of Model-Based Synthetic Air Data Estimators," *AIAA Guidance, Navigation, and Control Conference*, AIAA Paper 2015-0081, 2015. doi:10.2514/6.2015-0081

[4] Johansen, T. A., Cristofaro, A., SØrensen, K., Hansen, J. M., and Fossen, T. I., "On Estimation of Wind Velocity, Angle-of-Attack and Sideslip Angle of Small UAVs Using Standard Sensors," *2015 International Conference on Unmanned Aircraft Systems*, IEEE Publ., Piscataway, NJ, 2015, pp. 510–519. doi:10.1109/ICUAS.2015.7152330

[5] Wenz, A., Johansen, T. A., and Cristofaro, A., "Combining Model-Free and Model-Based Angle of Attack Estimation for Small Fixed-Wing UAVs Using a Standard Sensor Suite," *2016 International Conference on Unmanned Aircraft Systems*, IEEE Publ., Piscataway, NJ, 2016, pp. 624–632. doi:10.1109/ICUAS.2016.7502583

[6] Tian, P., and Chao, H., "Model Aided Estimation of Angle of Attack, Sideslip Angle, and 3D Wind Without Flow Angle Measurements," *2018 AIAA Guidance, Navigation, and Control Conference*, AIAA Paper 2018-1844, 2018. doi:10.2514/6.2018-1844

[7] Sun, K., Regan, C. D., and Egziabher, D. G., "GNSS/INS Based Estimation of Air Data and Wind Vector Using Flight Maneuvers," *2018 IEEE/ION Position, Location and Navigation Symposium*, IEEE Publ., Piscataway, NJ, 2018, pp. 838–849. doi:10.1109/PLANS.2018.8373461

[8] Klein, V., and Morelli, E. A., *Aircraft System Identification: Theory and Practice*, AIAA, Reston, VA, 2006, Chaps. 3, 6.

[9] Rossi, M., and Brunelli, D., "Autonomous Gas Detection and Mapping with Unmanned Aerial Vehicles," *IEEE Transactions on Instrumentation and Measurement*, Vol. 65, No. 4, 2016, pp. 765–775. doi:10.1109/TIM.2015.2506319

[10] Fravolini, M. L., del Core, G., Papa, U., Valigi, P., and Napolitano, M. R., "Data-Driven Schemes for Robust Fault Detection of Air Data System Sensors," *IEEE Transactions on Control Systems Technology*, Vol. 27, No. 1, Jan. 2019, pp. 1–15. doi:10.1109/TCST.2017.2758345

[11] Ossmann, D., "Enhanced Detection and Isolation of Angle of Attack Sensor Faults," *AIAA Guidance, Navigation, and Control Conference*, AIAA Paper 2016-1135, 2016. doi:10.2514/6.2016-1135

[12] Ossmann, D., Joos, H.-D., and Goupil, P., "Enhanced Sensor Monitoring to Maintain Optimal Aircraft Handling in Case of Faults,"

Journal of Guidance, Control, and Dynamics, Vol. 40, No. 12, 2017, pp. 3127–3137.
doi:10.2514/1.G002341

[13] Zeis, J. E. J., "Angle of Attack and Sideslip Estimation Using an Inertial Reference Platform," M.S. Thesis, U.S. Air Force Inst. of Technology, Wright-Patterson AFB, OH, June 1988.

[14] Colgren, R., "The Feasibility of Using an INS for Control System Feedbacks," *World Aviation Conference*, AIAA Paper 1998-5517, 1998.
doi:10.2514/6.1998-5517

[15] Colgren, R., Frye, M., and Olson, W., "A Proposed System Architecture for Estimation of Angle-of-Attack and Sideslip Angle," *Guidance, Navigation, and Control and Conference and Exhibit*, AIAA Paper 1999-4078, 1999.
doi:10.2514/6.1999-4078

[16] Colgren, R., and Martin, K., "Flight Test Validation of Sideslip Estimation Using Inertial Accelerations," *AIAA Guidance, Navigation, and Control Conference and Exhibit*, AIAA Paper 2000-4448, Aug. 2000.
doi:10.2514/6.2000-4448

[17] Colgren, R. D., "Method and System for Elimination and Correction of Angle of Attack and Sideslip Angle from Acceleration Measurements," Patent No. 6,273,370 B1 , Aug. 2001, http://www.freepatentsonline.com/6273370.html.

[18] Heller, S., Myschik, S., Holzapfel, F., and Sachs, G., "Low-Cost Approach Based on Navigation Data for Determining Angles of Attack and Sideslip for Small Aircraft," *AIAA Guidance, Navigation, and Control Conference and Exhibit*, AIAA Paper 2003-5777, 2003.
doi:10.2514/6.2003-5777

[19] Wise, K., "Flight Testing of the X-45A J-UCAS Computational Alpha-Beta System," *AIAA Guidance, Navigation, and Control Conference and Exhibit*, AIAA Paper 2006-6215, Aug. 2006.
doi:10.2514/6.2006-6215

[20] Myschik, S., Holzapfel, F., and Sachs, G., "Low-Cost Sensor Based Integrated Airdata and Navigation System for General Aviation Aircraft," *AIAA Guidance, Navigation, and Control Conference and Exhibit*, AIAA Paper 2008-7423, Aug. 2008.
doi:10.2514/6.2008-7423

[21] Murch, A., "A Flight Control System Architecture for the NASA AirSTAR Flight Test Infrastructure," *AIAA Guidance, Navigation, and Control Conference and Exhibit*, AIAA Paper 2008-6990, Aug. 2008.
doi:10.2514/6.2008-6990

[22] Karlgaard, C. D., and Schoenenberger, M., "Planetary Probe Entry Atmosphere Estimation Using Synthetic Air Data System," *Journal of Spacecraft and Rockets*, Vol. 55, No. 3, 2018, pp. 599–610.
doi:10.2514/1.A34115

[23] Morelli, E. A., "Real-Time Aerodynamic Parameter Estimation Without Air Flow Angle Measurements," *Journal of Aircraft*, Vol. 49, No. 4, 2012, pp. 1064–1074.
doi:10.2514/1.C031568

[24] Cho, A., Kim, J., Lee, S., and Kee, C., "Wind Estimation and Airspeed Calibration Using a UAV with a Single-Antenna GPS Receiver and Pitot Tube," *IEEE Transactions on Aerospace and Electronic Systems*, Vol. 47, No. 1, 2011, pp. 109–117.
doi:10.1109/TAES.2011.5705663

[25] Langelaan, J., Alley, N., and Neidhoefer, J., "Wind Field Estimation for Small Unmanned Aerial Vehicles," *Journal of Guidance, Control, and Dynamics*, Vol. 34, No. 4, 2011, pp. 1016–1030.
doi:10.2514/1.52532

[26] Lee, J. H., Sevil, H. E., Dogan, A., and Hullender, D., "Estimation of Maneuvering Aircraft States and Time-Varying Wind with Turbulence," *Aerospace Science and Technology*, Vol. 31, No. 1, 2013, pp. 87–98.
doi:10.1016/j.ast.2013.09.009

[27] Goshen-Meskin, D., and Bar-Itzhack, I. Y., "Observability Analysis of Piece-Wise Constant Systems. I. Theory," *IEEE Transactions on Aerospace and Electronic Systems*, Vol. 28, No. 4, 1992, pp. 1056–1067.
doi:10.1109/7.165367

[28] Goshen-Meskin, D., and Bar-Itzhack, I. Y., "Observability Analysis of Piece-Wise Constant Systems. 2. Application to Inertial Navigation In-Flight Alignment [Military Applications]," *IEEE Transactions on Aerospace and Electronic Systems*, Vol. 28, No. 4, 1992, pp. 1068–1075.
doi:10.1109/7.165368

[29] Rhee, I., Abdel-Hafez, M. F., and Speyer, J. L., "Observability of An Integrated GPS/INS During Maneuvers," *IEEE Transactions on Aerospace and Electronic Systems*, Vol. 40, No. 2, 2004, pp. 526–535.
doi:10.1109/TAES.2004.1310002

[30] Bageshwar, V. L., Gebre-Egziabher, D., Garrard, W. L., and Georgiou, T. T., "Stochastic Observability Test for Discrete-Time Kalman Filters," *Journal of Guidance, Control, and Dynamics*, Vol. 32, No. 4, 2009, pp. 1356–1370.
doi:10.2514/1.38128

[31] Krener, A. J., and Ide, K., "Measures of Unobservability," *Proceedings of the 48th IEEE Conference on Decision and Control*, IEEE Publ., Piscataway, NJ, 2009, pp. 6401–6406.
doi:10.1109/CDC.2009.5400067

[32] Hinson, B. T., Binder, M. K., and Morgansen, K. A., "Path Planning to Optimize Observability in a Planar Uniform Flow Field," *2013 American Control Conference*, IEEE Publ., Piscataway, NJ, 2013, pp. 1392–1399.
doi:10.1109/ACC.2013.6580031

[33] Hausman, K., Preiss, J., Sukhatme, G. S., and Weiss, S., "Observability-Aware Trajectory Optimization for Self-Calibration with Application to UAVs," *IEEE Robotics and Automation Letters*, Vol. 2, No. 3, 2017, pp. 1770–1777.
doi:10.1109/LRA.2017.2647799

[34] Dianetti, A. D., Weisman, R., and Crassidis, J. L., "Observability Analysis for Improved Space Object Characterization," *Journal of Guidance, Control, and Dynamics*, Vol. 41, No. 1, 2018, pp. 137–148.
doi:10.2514/1.G002229

[35] Ghilani, C., *Adjustment Computations: Spatial Data Analysis*, 5th ed., Wiley, Hoboken, NJ, 2010, pp. 89–90, Chap. 6.

[36] Gleason, S., and Gebre-Egizabher, D., *GNSS Applications and Methods*, Artech House, Norwood, MA, 2009, pp. 149–172, Chap. 6.

[37] Berman, Z., and Powell, J. D., "The Role of Dead Reckoning and Inertial Sensors in Future General Aviation Navigation," *IEEE 1998 Position Location and Navigation Symposium*, IEEE Publ., Piscataway, NJ, 1998, pp. 510–517.
doi:10.1109/PLANS.1998.670206

[38] Xing, Z., "Over-Bounding Integrated INS/GNSS Output Errors," Ph.D. Thesis, Univ. of Minnesota, Twin Cities, Minnesota, MN, Sept. 2010.

[39] Gracey, W., "Measurement of Aircraft Speed and Altitude," NASA TR 1046, May 1980.

[40] Golub, G., and van Loan, C., *Matrix Computations*, Johns Hopkins Univ. Press, Baltimore, MD, 2013, pp. 71–73, Chap. 2.

[41] Taylor, W., "Aircraft Simulation Baseline 2014 v1," Univ. of Minnesota's Digital Conservancy Minnesota, 2014, http://hdl.handle.net/11299/163868 [retrieved Sept. 2018].

[42] Dorobantu, A., Johnson, W., Lie, F. A., Taylor, B., Murch, A., Paw, Y. C., Gebre-Egziabher, D., and Balas, G., "An Airborne Experimental Test Platform: From Theory to Flight," *2013 American Control Conference*, IEEE Publ., Piscataway, NJ, 2013, pp. 659–673.
doi:10.1109/ACC.2013.6579912

[43] Owens, B., Cox, D., and Morelli, E., "Development of a Low-Cost Sub-Scale Aircraft for Flight Research: The FASER Project," *25th AIAA Aerodynamic Measurement Technology and Ground Testing Conference*, AIAA Paper 2006-3306, June 2006.
doi:10.2514/6.2006-3306

[44] "Rosemount Model 858 Flow Angle Sensors," Rosemount, Bulletin 1014, Burnsville, MN, 1988.

[45] Parameswaran, V., Jategaonkar, R., and Press, M., "Five-Hole Flow Probe Calibration from Dynamic and Tower Flyby Maneuvers," *Journal of Aircraft*, Vol. 42, No. 1, 2005, pp. 80–86.
doi:10.2514/1.5708